uOttawa

L'Université canadienne
Canada's university

FACULTÉ DES ÉTUDES SUPÉRIEURES ET POSTOCTORALES

uOttawa

L'Université canadienne
Canada's university

FACULTY OF GRADUATE AND POSDOCTORAL STUDIES

Craig Holvey
AUTEUR DE LA THÈSE / AUTHOR OF THESIS

M.A.Sc. (Chemical Engineering)
GRADE / DEGREE

Department of Chemical Engineering
FACULTÉ, ÉCOLE, DÉPARTEMENT / FACULTY, SCHOOL, DEPARTMENT

Characterization of Microreactors with Respect to Pressure Drop, Heat Transfer and Mixing Efficiency

TITRE DE LA THÈSE / TITLE OF THESIS

Arturo Macchi
DIRECTEUR (DIRECTRICE) DE LA THÈSE / THESIS SUPERVISOR

CO-DIRECTEUR (CO-DIRECTRICE) DE LA THÈSE / THESIS CO-SUPERVISOR

B. Kruczek

Jason Zhang

Gary W. Slater
Le Doyen de la Faculté des études supérieures et postdoctorales / Dean of the Faculty of Graduate and Postdoctoral Studies

# Characterization of Microreactors with Respect to Pressure Drop, Heat Transfer and Mixing Efficiency

By Craig Holvey

Thesis submitted to the

Faculty of Graduate and Postdoctoral Studies

In partial fulfillment of the requirements

For the Master of Applied Science in Chemical Engineering

Department of Chemical and Biological Engineering

University of Ottawa

*Your file Votre référence*
*ISBN:* 978-0-494-66233-5
*Our file Notre référence*
*ISBN:* 978-0-494-66233-5

## Abstract

Microreactors have been shown to greatly improve process in the pharmaceutical and fine chemical industry and provide solutions to many of the drawbacks that exist in batch and semi-batch processes. However, industry experts agree that there is a need for a standard method of analysis to compare the performance of complex microreactor geometries. This study provides a method to compare the pressure drop and mixing efficiency on a common scale and observes the effect of reactor materials on the overall heat transfer. Semi-empirical pressure drop modeling determined the pressure drop along the mixing zone and showed that the axial mixing of the tangential mixing unit had the highest friction factor. Mixing efficiency was characterized using the 4$^{th}$ Bourne reaction and showed that under turbulent conditions at a given energy dissipation the mixing efficiency is independent from geometry and confirmed that their mixing occurs at the same mixing time scale. However, after increasing the viscosity of the system, the geometries differed in their transition from turbulent to laminar. The tangential mixing unit showed to have lowest regime transition Reynolds number. The effect of reactor materials was observed with respect to heat transfer performance. Empirical modeling determined that the Hastelloy reactor provided a heat transfer rate up to 40% greater than a glass system and was limited by the convective heat transfer of the reactor channels whereas the glass reactor was limited by the thermal conductivity of the reactor wall.

## Sommaire

Les microréacteurs ont permis d'améliorer grandement les procédés de l'industrie pharmaceutique et de la chimie fine et de fournir des solutions à plusieurs inconvénients qui existent avec les réacteurs en cuvés et semi-cuvés. Toutefois, les experts de l'industrie conviennent qu'il y a un besoin pour une méthode d'analyse standard pour comparer les performances des microréacteurs avec géométries complexes. Cette étude fournit une méthode afin de comparer la chute de pression et l'efficacité de mélange sur une échelle commune et observe l'effet des matériaux du réacteur sur le transfert de chaleur globale. À partir d'une modélisation semi-empirique des chutes de pression, la chute de pression dans la zone de mélange a été déterminée et le model a montré que le mélange axial d'une unité de mélange tangentiel avait le plus haut coefficient de frottement. L'efficacité de mélange a été caractérisée par la 4$^{e}$ réaction Bourne. Dans des conditions de mélange turbulent et pour une énergie dissipée donnée, l'efficacité est indépendante de la géométrie et confirme que le mélange se produit à la même échelle de temps. Toutefois, après une augmentation de la viscosité du système, les géométries diffèrent dans leurs régime de mélange allant de turbulent à laminaire. L'unité de mélange tangentielle a le plus bas nombre de Reynolds au point de transition régime. L'effetdes matériaux du réacteur a été observé à l'égard de la performance de transfert de chaleur. À partir d'une modélisation empirique, le model montre que le réacteur en Hastelloy fourni un taux de transfert de chaleur jusqu'à 40% plus élevée qu'un système en verre. De plus le taux de transfert de chaleur du réacteur en Hastelloy est limité par le transfert de chaleur par convection dans les canaux du réacteur alors que le réacteur en verre est limité par la conductivité thermique de la paroi du réacteur.

# Table of Contents

## List of Figures

## List of Tables

## Acknowledgments

I would like to first thank my professors Dr. Arturo Macchi and Dr. Dominique Roberge for the opportunity to study microreactor technology.

I would like to thank the LONZA Exclusive Synthesis group for their support in the experimental setup an analysis. I would also like to thank Siemens Automation group for their support with the use of the Siemens SiProcess.

I finally like to thank my family and friends for their support during my studies. A special thanks to Brenna Holvey for her support in the writing of this thesis.

# Chapter 1. Introduction

Recent social developments such as increased environmental awareness and a decrease in the financial economy have caused the fine chemical and pharmaceutical industry to shift towards more efficient processes. Process intensification is quickly becoming an important aspect of the optimization and design of fine chemicals and active pharmaceutical ingredients (API). Hundreds of microreactors with different geometries have been created to meet the increased demand for a more intense process. Several studies have attempted to provide quantification techniques for these complex geometries. Quantification methods within these studies include the use of "chemical rulers" to understand the mixing of a particular geometry by the analysis of the yield or selectivity of a particular reaction scheme (Baldyga, et al., 1999; Bourne, et al., 1991; Bourne, et al., 1992). There are also several studies that attempt to characterize the transport phenomena in complex geometries which include CFD modeling and the use of semi-empirical dimensional analysis (Kockmann, et al., 2006; Ottino, et al., 1979). Despite the large amount of research in this field, there is a consensus among industry experts that there is a need for a standard method of analysis to compare the performance of complex microreactor geometries (Falk, et al., 2010; Kukukovaa, et al., 2009). The effect of geometry plays an important role in the pressure loss, mixing efficiency and heat transfer, of a particular process. However, it's unclear how currently used geometries are used to optimize these aspects and whether they have an advantage over other geometries.

Industrial standards in the production of fine chemicals and APIs typically consist of semi-batch reactor trains where the process is controlled by the dosage rate of one component. Semi-batch processes are currently considered as the industrial standard due to their modularity and availability. However, low heat transfer rates and imperfect mixing in the reactor vessel create an inefficient process which is often considered to be overdesigned. Other difficulties with semi-batch processes include the use of large volumes of solvent and safety hazards common with the use of large vessels. These process difficulties also suggest economic implications such as increased capital and operational costs.

## 1.1. Microreactor Technology

Microreactors provide solutions to many of the drawbacks that exist in batch and semi-batch processes. A microreactor consists of a series of reactor plates, which are interchangeably placed between heat exchange plates. Reactor plates each consist of a small channel with three zones: the mixing zone, the main channel and the entrance/exit (Figure 1.1). These channels create efficient heat transfer and therefore allow for a greater degree of process intensification.

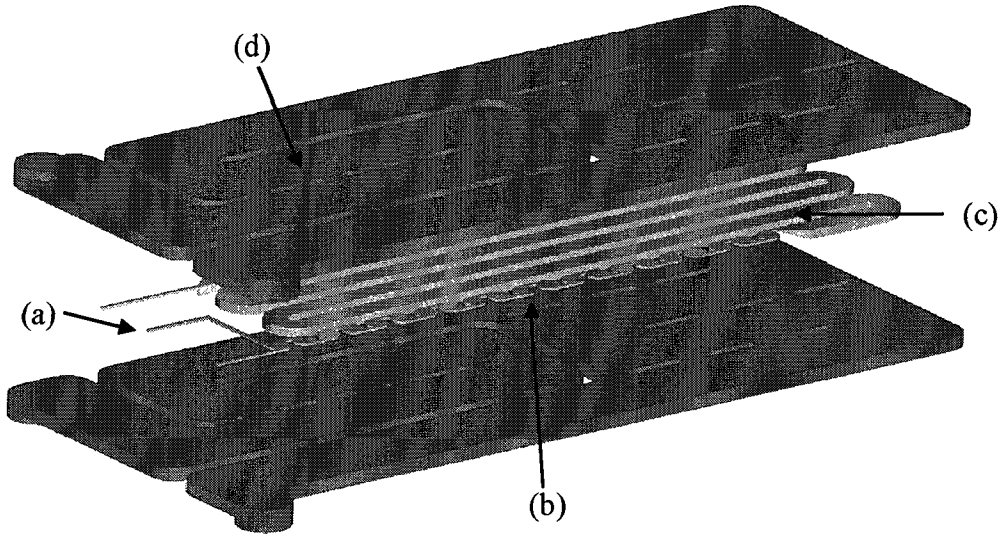


**Figure 1.1: General microreactor setup; (a) entrance and exits , (b) mixing zone, (c) main channel, (d) heat exchange channels**

Studies show that half of reactions used by the pharmaceutical and fine chemical industry can benefit from continuous microreactor technology (Roberge, et al., 2005). Applicable reactions are separated into class I, II or III (Roberge, 2004). Class I reactions are limited by the rate of molecular interaction. These reactions generally occur in the mixing zone and can produce local hotspots. Superior mixing structures in a microreactor can improve yields in class I reaction by reducing the mixing time. The relatively small dimensions and resulting high heat transfer rates in the main channel would also prevent hotspot formation. Class II reactions have longer reaction times and are considered to be kinetically controlled. These types of reactions would not benefit from a particular mixing geometry as they are not limited by their rate of contact efficiency. However, high heat transfer rates of microreactors would still provide an added benefit over batch processes. Class III reactions are slow reactions and therefore large residence times are required to achieve equilibrium. Class III reactions would also benefit from the heat transfer

capabilities of a microreactor in cases where a thermal hazard, like autocatalytic reactions, is present.

This study examines three different reactor geometries that create secondary flows and enhance mixing in different ways. The tangential mixing structure in figure 1.2(a) creates recirculation zones on each side of the structure while creating a streamline effect through the center as the path of least resistance (Jongkwang, et al., 2009). The SZ mixing structure in figure 1.2(b) promotes mixing through the generation of dean flow by creating vortices perpendicular to the direction of flow (Rosaguti, et al., 2004). Dean flow is often quantified by the dimensionless Dean Number (De) in equation 1.1. Where, Re, represents the Reynolds number; D is the channel diameter and, r, represents the radius of curvature.

$$De = Re\left(\frac{D}{2r}\right)^{0.5} \qquad (1.1)$$

The caterpillar mixing structure in figure 1.2(c) creates a split and recombine flow pattern (Lee, et al., 2008). This effect reduces the diffusion length by splitting and stretching the lamellae (Schönfeld, et al., 2004).

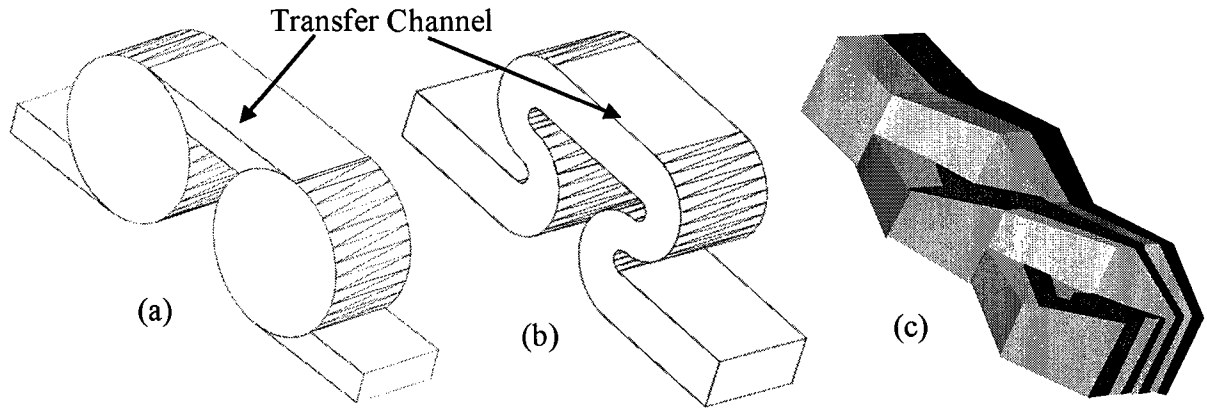


**Figure 1.2: Different mixing geometries; (a) Tangential mixer (TG), (b) SZ mixing channel (SZ), (c) Caterpillar mixing geometry (CAT)**

This study uses multiple reactors to analyze the effect of a variety of geometries on the pressure drop, mixing efficiency and heat transfer of the system. To account for the channel size, three different reactor sizes were used. These sizes are based on a scaling factor which are in order from smallest to largest; 300 series, 200 series and 100 series. In order to characterize the individual components of a microreactor; a proper representation of the characteristic length is required. Main channels can be represented by their cross-sectional areas and hydraulic diameters since they remain constant throughout the channel length. Due to the fact that mixing zones vary in shape, characteristic dimensions must be justified. The SZ and CAT mixing structures can be characterized by their smallest dimensions because this is where the largest pressure drop is created and the variation of the channel size is relatively small. In the case of the TG mixing structure, we encounter a large variation in the cross sectional area and therefore the transfer channel dimensions between mixing elements would be unrepresentative of the secondary flows created by the geometry.

To determine to characteristic length of the TG mixing unit, the surface area of a mixing unit is determined and an average is calculated over the length of one repeated unit. The average channel height can then be used to determine a representative hydraulic diameter. The surface area used to determine the average height of a TG mixing unit is shown in figure 1.3 and detailed calculations for this surface area can be found in Appendix B2. Dimensions such as volume and hydraulic diameters used for mixing zones in figure 1.2 can be found in Appendix A.

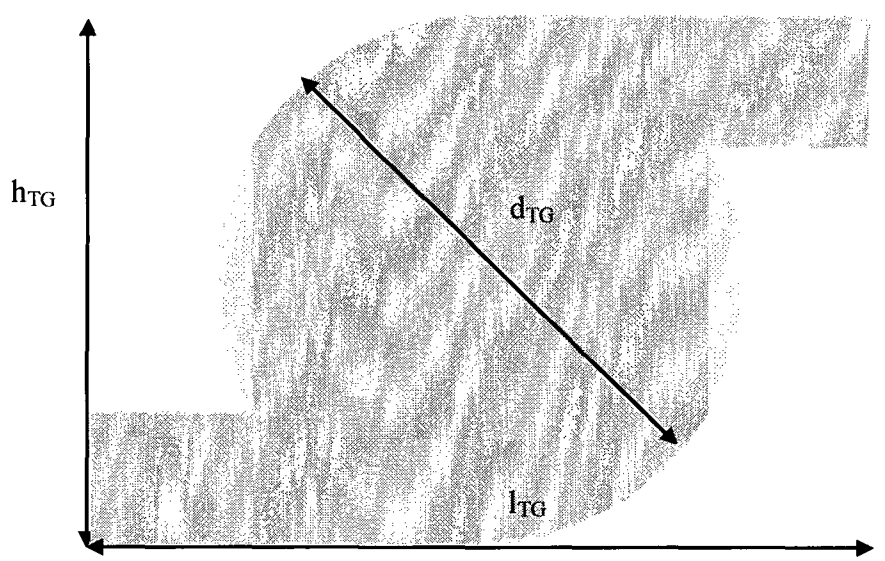


**Figure 1.3: Representation of surface area integrated for the determination of the average cross sectional area. Grey areas show the integrated area, $h_{TG}$ is the mixing unit height, $l_{TG}$ is the mixing unit length and $d_{TG}$ is the diameter of the mixing area.**

## 1.2. Objectives

The objective of this study was to characterize and compare the TG, SZ and CAT mixing microstructures. In order to effectively characterize these mixing structures, first the pressure drop is required. The pressure drop along the mixing zone represents the energy input and indicates the degree of turbulence in the system. In Chapter 2, the pressure drop across several plates with various components and geometries is modeled to estimate the friction factors of the individual components. In Chapter 3, this study then compares three mixing micro structures with respect to their mixing efficiency. Geometry plays a key role in increasing the mixing intensity and reducing the time scale of mixing.

Heat transfer of the microreactor is also an important operational aspect. In Chapter 4, two microreactors with similar geometries but made of glass and Hastelloy are used to determine and model the effects of material conductivity on the individual types of heat transfer occurring in the microreactor. Finally conclusions and recommendations for future research are presented in Chapter 5.

# Chapter 2. Pressure Drop Analysis

## 2.1. Pressure Drop Modelling

In order to determine the pressure drop along the mixing zone, the pressure drop along the entire plate is first determined. Then by using a variation of microreactor plates with various dimensions, sizes and components (i.e. plates without mixing zones) each section could be decoupled and characterized using friction factors. To characterize the pressure drop (ΔP) of individual components of a reactor plate, we apply the classical definition of friction factors (2.1) to the Bernoulli equation (deNevers, 2005) to create a standard pressure drop model (2.2) which incorporates laminar (λ) and turbulent (ω) friction factors.

$$F \equiv 4f\frac{\Delta l}{d}\cdot\frac{u^2}{2} \tag{2.1}$$

$$\Delta P = \sum\left(\lambda_i\frac{l_i}{d_{h,i}} + \omega_i\frac{l_i}{d_{h,i}}\right)\cdot\frac{\rho}{2}u^2{}_{Ref,i} \tag{2.2}$$

The laminar friction factor is dependent solely on the Reynolds number and equation 2.2 can be expanded to solve for the pressure drop of an individual component (2.3). The final model will consist of 6 factors; two factors for each of the three reactor components discussed in chapter 1.1(main channel, mixing zone and entrance/exit). Lengths of each section in a reactor plate are the quotient of the volume to the cross-sectional area. Further details related to the volume calculations can be found in Appendix B1.

$$\Delta P_i = C_{f,i}\frac{u_{Ref,i}\mu l_i}{2\cdot d_{h,i}^{\ 2}} + \omega_i \frac{u^2{}_{Ref,i}\rho l_i}{2\cdot d_{h,i}} \tag{2.3}$$

The system of equations solves for the friction factors by applying MATLAB's linear regression solver. MATLAB provides the friction factors, correlation coefficient and a 95% confidence interval for each factor to assess its significance. The friction factors are then isolated based on equation 2.4 since the velocity will factor out by applying the Reynolds number.

$$\Delta P_{Total} = \sum_i \left(\frac{C_{f,i}}{Re_i}\frac{l_i}{d_{h,i}} + \omega_i \frac{l_i}{d_{h,i}}\right)\cdot \frac{\rho}{2} u_{ref,i}{}^2 \tag{2.4}$$

The overall friction factor ($f$) of each component is determined in equation 2.5

$$f_i = \frac{C_{f,i}}{Re_i} + \omega_i \tag{2.5}$$

A Moodie plot is then used to organize and compare the resulting friction factors.

## 2.2. Experimental Setup

The pressure drop experiments were performed at ambient temperature using water as the process fluid. The pressure drops along the reactor plates were observed at the inlet and outlet of the reactor. Flow rates were varied using a gear pump which was controlled by a coriolis meter (Figure 2.1). The coriolis meters are an ideal sensor as a mass flow indicator because the fluids have a constant density (Reizner, 2004). Both the pressure drop and mass flow rates were monitored using the online control system of Siemens PCS-7.

Process fluid flow rates ranged from 20 to 450 g/min. Series 100 and 200 trials were performed at lower flow rates, ranging from 20 to 200 g/min.

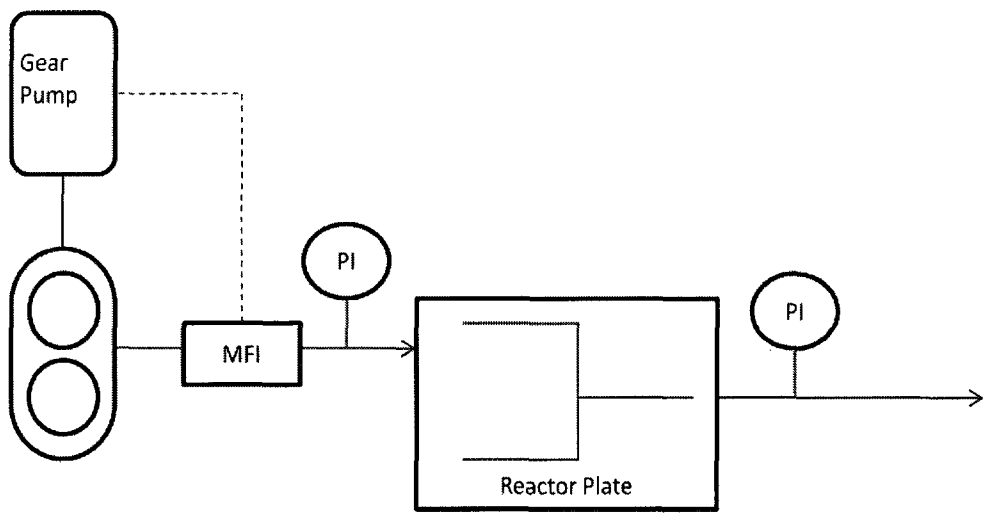


**Figure 2.1: Experimental setup for pressure drop experiments, PI : Pressure Sensor, MFI: mass flow meter (coriolis meter)**

## 2.3. Results and Discussion

Figures 2.2 to 2.4 represent the pressured drop of several reactor plates and residence time modules at the flow rates described in chapter 2.2. The flow rate is increased by raising the power input to the pump, which causes both the pressure drop and the energy dissipation to increase. The six factor model presented an excellent fit to the experimental data for all series. Correlation coefficients exceeded 0.997. The lowest correlation coefficient was observed in the 100 series plates and was likely due to the reactor plate 102 and FJZ-1, which has the same geometry but resulted in a slightly different pressure drop.

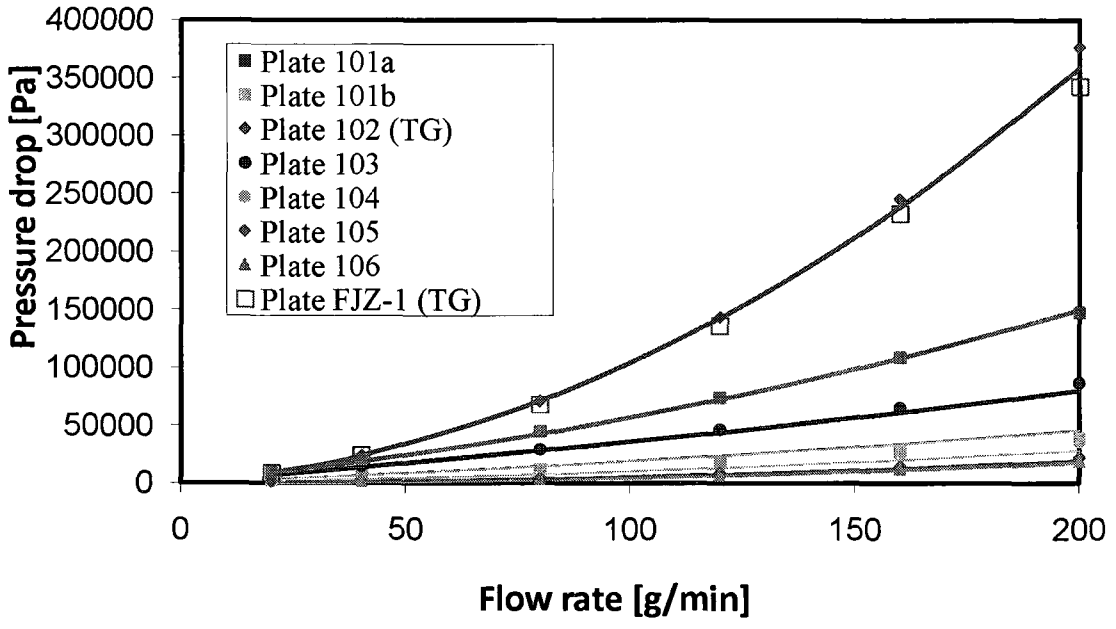


Figure 2.2: Pressure drop experimental data (points) and model (lines) for various 100 series reactor plates (TG) represents a tangential mixing unit and (CAT) represents a catepillar mixing unit.

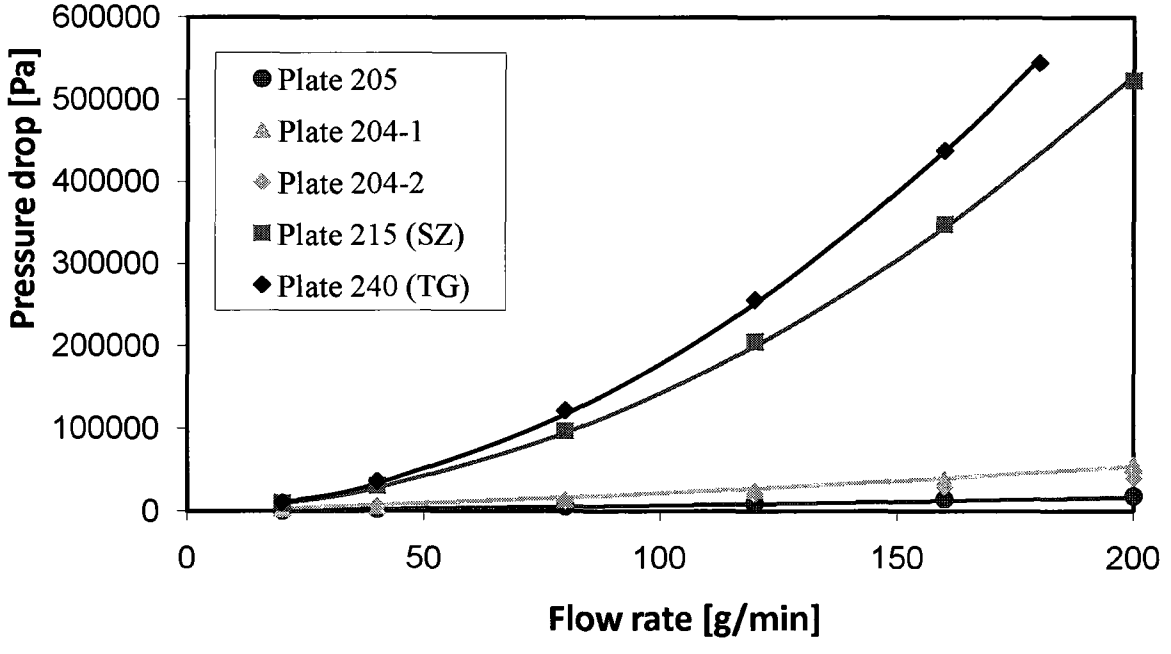


Figure 2.3: Pressure drop experimental data (points) and model (lines) for various 200 series reactor plates (TG) represents a tangential mixing unit and (SZ) represents an SZ shaped mixing unit.

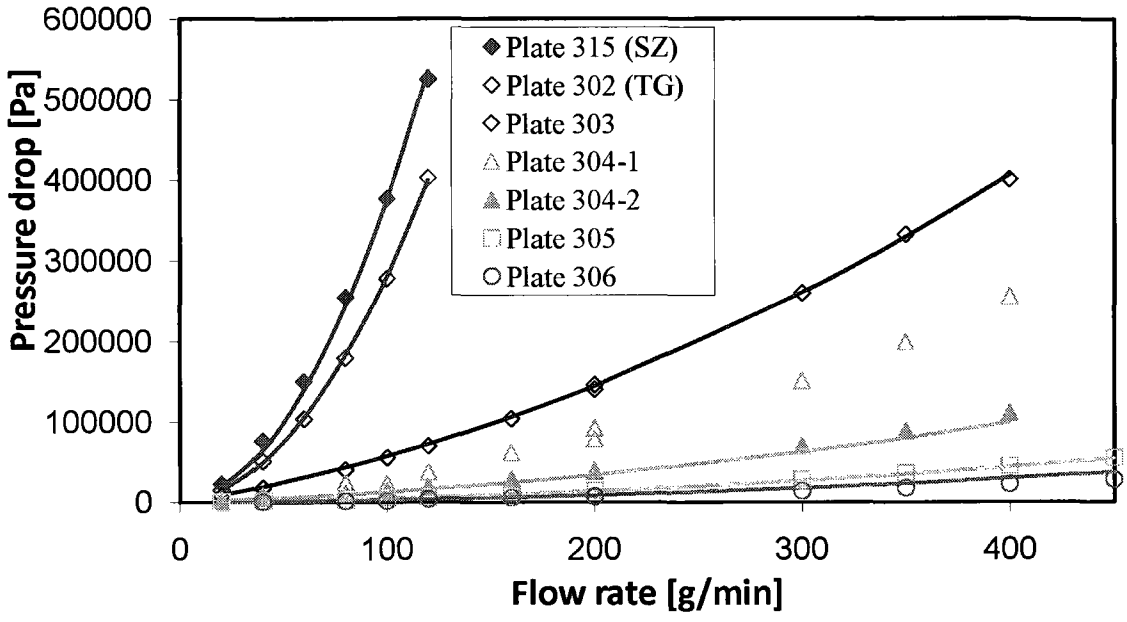


**Figure 2.4: Pressure drop experimental data (points) and model (lines) for various 300 series reactor plates (TG) represents a tangential mixing unit and (SZ) represents SZ shaped mixing unit.**

When referring to equation (2.3), different flow regimes will provide a different relationship between the superficial velocity and pressure drop. From figures 2.2 to 2.4, plates with mixing zones have a non-linear relationship to the flow rate, suggesting that the pressure drop is proportional to the velocity squared and that flow is akin to turbulence. However, plates without mixing structures show very little curvature, suggesting that there is a directly proportional relationship to the velocity and that the flow is dominated by shear or laminar friction. The friction factor values in table 2-1 support these observations.

Table 2-1: Modeled laminar and turbulent friction factors and the correlation coefficient for the model of each series (6 factor model).

| Series: | 100 Series | | 200 Series | | 300 Series | |
|---|---|---|---|---|---|---|
| | $C_f$ | $\omega$ | $C_f$ | $\omega$ | $C_f$ | $\omega$ |
| Main channel | 89.51 | - | 39.13 | 0.08 | 45.45 | 0.03 |
| Mixing zone **TG** | - | 10.68 | 1632 | 13.75 | - | 9.90 |
| Mixing zone **CAT** | 114.19 | 0.16 | N/A | N/A | N/A | N/A |
| Mixing zone **SZ** | N/A | N/A | 78.83 | 0.27 | 80.19 | 0.28 |
| Entrance/Exit | - | 0.19 | 1.70 | - | 115.07 | 0.04 |
| ($R^2$) | **0.9968** | | **0.9995** | | **0.9995** | |

Despite the excellent fit of the 6 factor model with $R^2$ values greater than 0.997, there is a lack of sensitivity with several constants. The 95% confidence interval of the constants, presented in figures 2.5 to 2.7, provide an indication as to which constants can be removed.

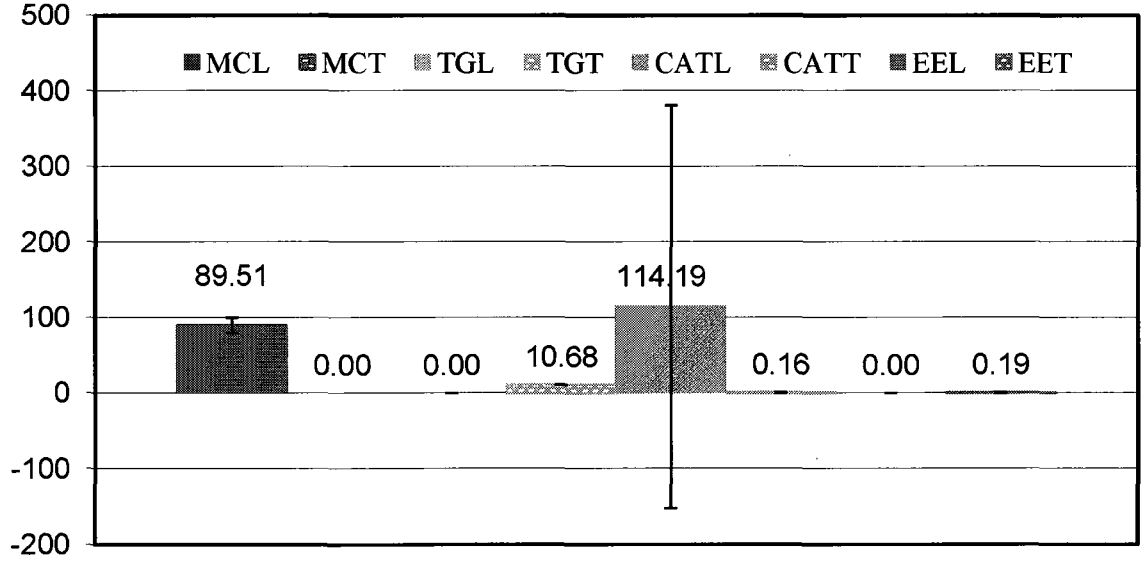


Figure 2.5: Confidence Interval (95%) for the 100 series modeled constants. Prefixes: MC represent the main channel, TG represent tangential mixing units, CAT represent caterpillar mixing units, EE represent entrances and exits. Suffixes: L represents the laminar term and T represents the turbulent term.

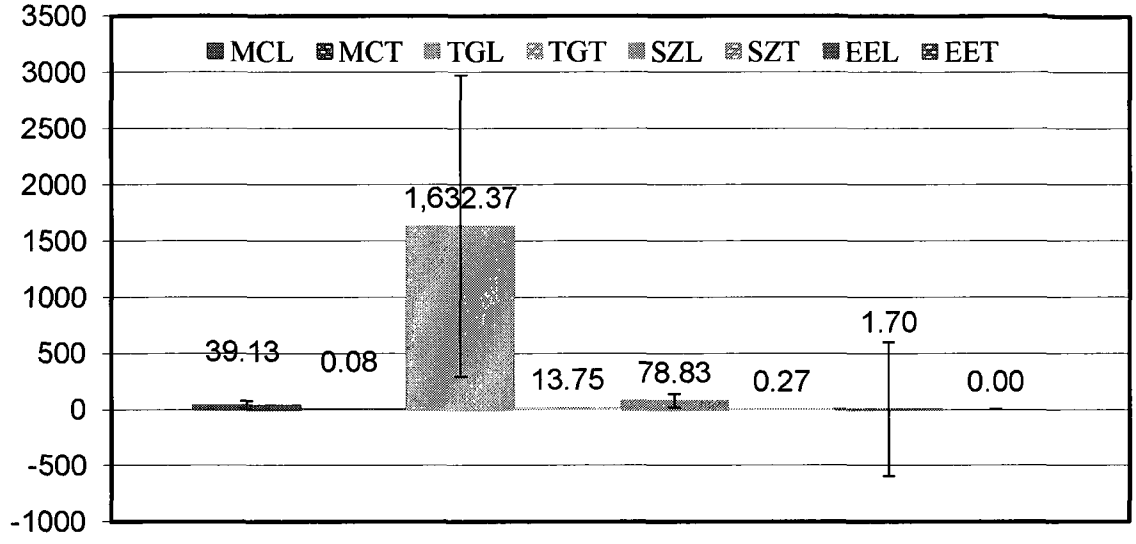


Figure 2.6: Confidence Interval (95%) for the 200 series modeled constants. Prefixes: MC represent the main channel, TG represent tangential mixing units, SZ represent SZ shaped mixing units, EE represent entrances and exits. Suffixes: L represents the laminar term and T represents the turbulent term.

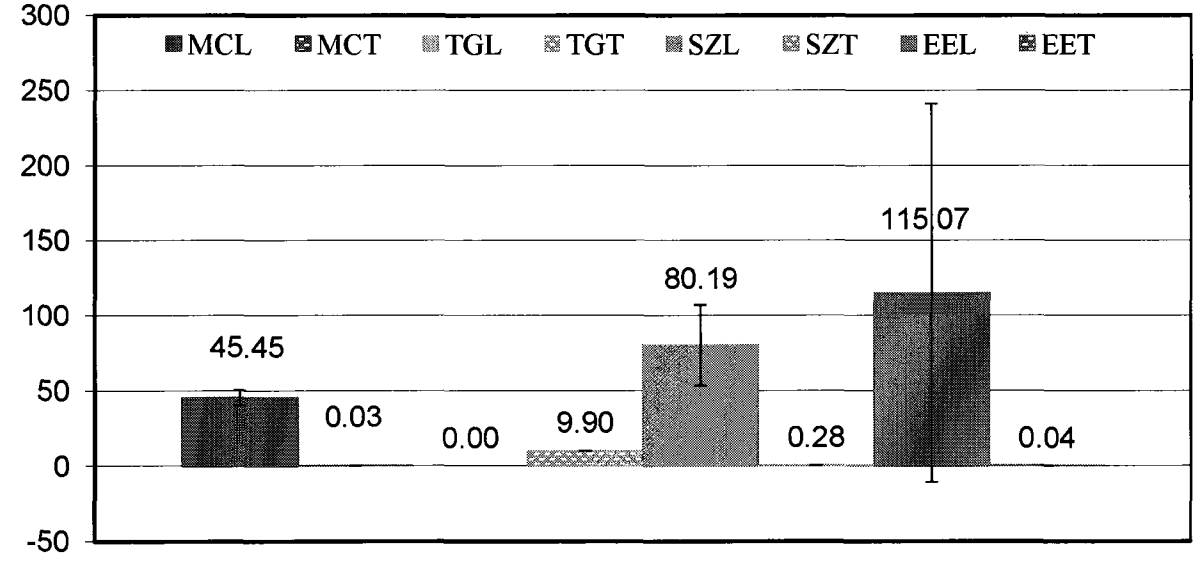


Figure 2.7: Confidence Interval (95%) for the 300 series modeled constants. Prefixes: MC represent the main channel, TG represent tangential mixing units, SZ represent SZ shaped mixing units, EE represent entrances and exits. Suffixes: L represents the laminar term and T represents the turbulent term.

Laminar terms associated with the mixing zones as well as entrances and exits, both have very large confidence intervals and have an insignificant effect on the model response. The removal of the laminar terms from the model shows that these sections are dominated by turbulence. Assuming flow regime laws are not changed in microstructures (Falk & J.-M.Commenge., 2010), the critical Reynolds number for transition from laminar to turbulent flow will be approximately 2000. The turbulence observed in the mixing zones must therefore be a response to the formation of secondary flows akin to turbulence, since Reynolds numbers reach a maximum of 2200. The relatively small dimensions of the entrances and exit produce higher velocities at a given flow rate. The Reynolds numbers of the entrances and exits range from 200 to 5000, therefore there is indeed turbulence at higher flow rates. However, this does not explain why laminar effects are insignificant through the entire range of flow rates. The entrance and exit effects may still be linked to the main channel because all plates have an entrance and therefore these effects are difficult to decouple. Moreover their contribution to the overall pressure drop is relatively small due to the short length.

The turbulent friction factors of the main channel have relatively small magnitudes with large confidence intervals. This suggests that these factors have an insignificant effect on the pressure drop of the main channel. This also agrees with the proposed design of the main channels. These main channels have large aspect ratios (ratio of channel height to channel width) which prevent dean flow and therefore have low secondary flow formation leading to a lower degree of turbulence.

The summary of the reduced model (table 2-2) justifies the claims discussed above. Entrance and exit laminar effects were insignificant based on their confidence intervals. Laminar terms of the mixing zones also had very large confidence intervals and were removed. Finally, the main channel turbulent terms for the 100 and 200 series were removed without a significantly reducing the overall model fit. The correlation coefficients of the reduced model were comparable to the six factor model.

**Table 2-2: Experimentally determined laminar and turbulent friction factors and the correlation coefficient for the model of each series after the model has been reduced.**

| Series: | 100 series | | 200 series | | 300 series | |
|---|---|---|---|---|---|---|
| | $C_f$ | $\omega$ | $C_f$ | $\omega$ | $C_f$ | $\omega$ |
| Main channel | 90.91 | - | 79.57 | - | 49.29 | 0.03 |
| Mixing zone **TG** | - | 10.65 | - | 15.29 | - | 9.91 |
| Mixing zone **CAT** | - | 0.20 | N/A | N/A | N/A | N/A |
| Mixing zone **SZ** | N/A | N/A | - | 0.31 | - | 0.33 |
| Entrance/Exit | - | 0.19 | - | 0.26 | - | 0.06 |
| ($R^2$) | **0.9967** | | **0.9993** | | **0.9994** | |

One exception to the reduced model reduction was found in the 300 series main channel as both laminar and turbulent terms were required to sustain a correlation coefficient greater than 0.997. This may be due to increased velocities caused by smaller channel geometries and greater flow rates. Experimental trials for the 300 series reactors produced Reynolds numbers exceeding 2200. The fluid would thus be flowing in a transitional regime, where both the laminar and turbulent terms will be significant.

In order to rationalize and compare these friction factors, they must be validated by exterior relationships. Table 2-3 presents the main channel friction factors and compares them to the theoretical values for rectangular channels under laminar conditions (Kockmann, 2008).

**Table 2-3: Comparison of experimentally determined friction factors to calculated values**

| **Series** | **100s** | **200s** | **300s** |
|---|---|---|---|
| Theoretical | 87.18 | 76.86 | 79.52 |
| Experimental | 90.91 | 79.57 | 49.29 |
| %Difference | 4.28% | 3.52% | 38.02% |

The friction factor values extracted by the semi-empirical model compare to the theoretical values within a 5% difference. The one exception to this trend is the 300 series, which was shown to produce some degree of turbulence in the main channel.

The friction factors of the reduced model are organized in figure 2.8 as a Moodie plot which allows for comparison. Tangential mixing (TG) units create the largest friction with a turbulent friction factor greater than 9.0. The TG mixing unit produces the most abrupt changes in the velocity field as shown by the creation of recirculation zones and dead spots to dissipate energy (Yung-Chiang Chung, 2004). Indeed, the rate of frictional dissipation must be high in order to create axial vortices acting opposite to the direction of flow. SZ mixing units produce a turbulent friction factor of approximately 0.3 due to the formation of dean vortices. Since there are no recirculation zones or dead spots, as seen in the TG mixer, the frictional forces acting on the fluid are lower.

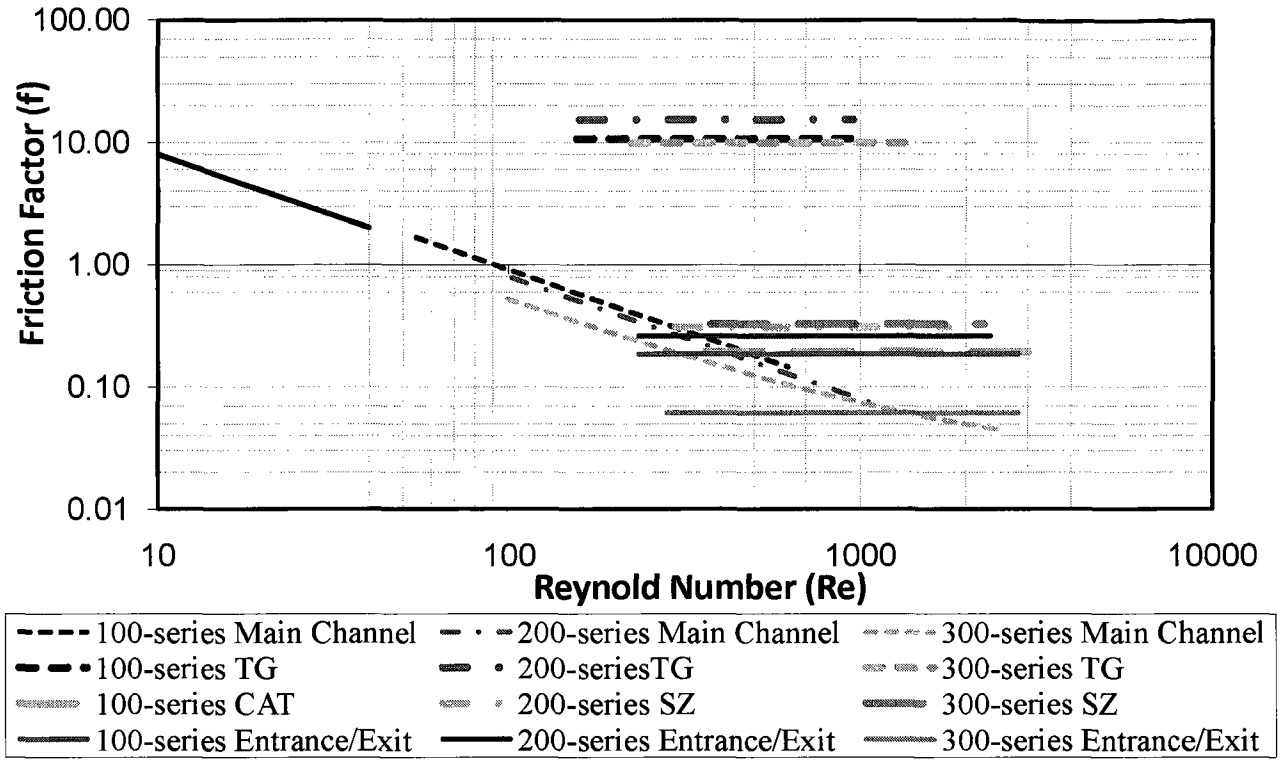


**Figure 2.8: Moodie plot, for the individual components of the 100, 200 and 300 series reactor plates.**

The mixing structure with the lowest friction factor is the Caterpillar (CAT) mixing structure, with a friction factor of 0.2. Similar to the SZ mixer, the CAT mixing structure creates mixing in the direction of flow but uses a split and recombine concept instead of deans vortices. The lack of bending in the channel produces lower angles of incidence with the channel wall and therefore has a lower friction factor. Both SZ and CAT mixing zones exist in the same frictional range of the entrance and exit zones.

The pressure drops of the reactor plates in this study are generally dominated by the mixing zone pressure drop. Factors such as the channel size, mixing zone length, and geometry play a role in the overall pressure drop. Figures 2.9 and 2.10 show the percentage

of the overall pressure drop each mixing zone has on a reactor plate and how it compares to the main channel. The entrance and exits have a small effect on the overall pressure drop and are therefore not included.

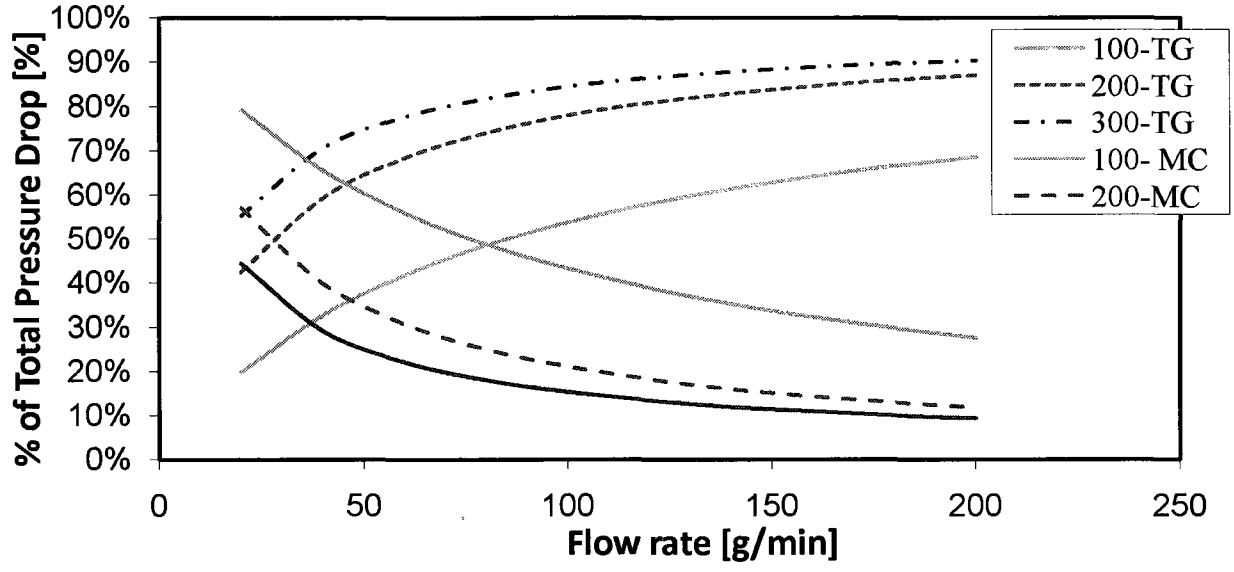


**Figure 2.9: Percentage of pressure drop associated with the TG mixing plates and the associated main channels (MC), based on the reduced model.**

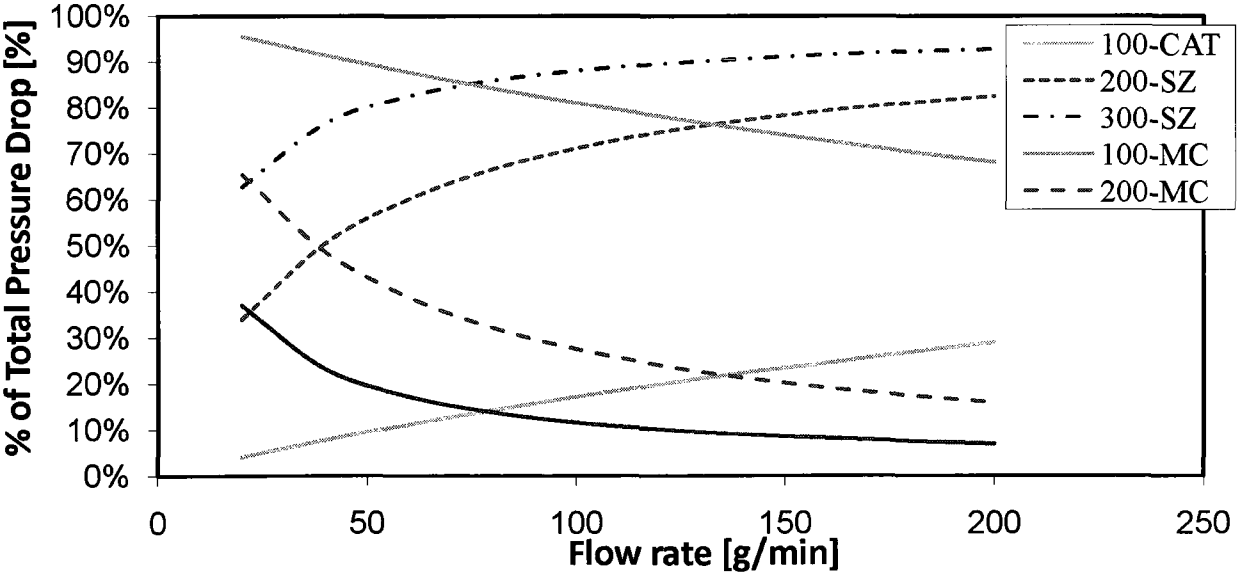


**Figure 2.10: Percentage of pressure drop associated with the SZ and CAT plates and the associated main channels(MC) , based on the reduced model.**

The percentage of the pressure drop associated with the mixing zone increases along with the flow rate. This is due to the fact that the pressure drop in the mixing zone increases proportionally to the velocity squared, whereas the pressure drop in the main channel increases directly proportional to the velocity. The channel size also affects the dominant pressure drop zones in the reactor plate. Smaller channels will have higher Reynolds numbers due to a higher velocity at a given flow rate, which leads to a higher degree of turbulence. This effect can be seen in both figures 2.9 and 2.10 where the 200 and 300 series mixing zones dominate at lower flow rates. The difference in percentage of total pressure is not apparent between the TG and SZ mixing zones in a given series because they are both dominant throughout the entire experimental range. However, the main channel pressure drop is dominant in cases where a CAT mixing structure is being used. While the CAT mixing structure had the lowest friction factor, comparable to entrance and exit lines of similar dimensions, it is more likely that this effect is due to a reduced mixer length, which was much short than the other mixing zones examined in this study. A shorter mixing length reduces the pressure drop associated with the component which reduces its effect on the overall pressure drop.

# Chapter 3. Mixing Efficiency Analysis

Through the use of friction factor modeling it is now known how friction in a microreactor is created. Due to the fact that the geometry has an effect on the friction in the system, it is hypothesized that the geometry will also have an effect on the mixing of the system. In order to understand and control mixing in a microreactor, it must be quantified in a way that allows for an effective comparison between different shapes and flow fields. This chapter focuses on the quantification of mixing using "chemical rulers" to compare mixing effects of different microreactor geometries (figure 1.2) on a common scale.

## 3.1. Mixing Quantification

The ability to control the mixing in a system is an important aspect of a reactor. There exists several studies that discuss different techniques and units to quantify mixing (Falk & Commenge., 2010; Baldyga, 1998; Ottino, Ranz, et al., 1979; Kockmann, et al., 2006). Many of these studies agree with the use of a characteristic mixing time to quantify mixing of a system. The mixing time in a reactor consists of three different time scales (see figure 3.1).

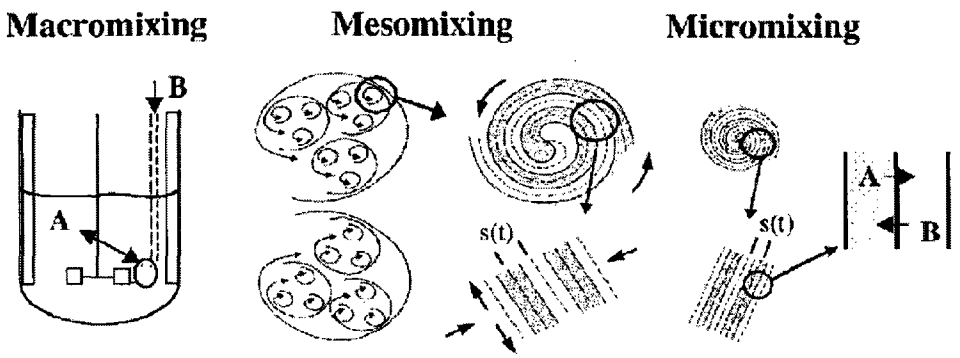


Figure 3.1: Three main mixing time scales (Johnson, et al., 2003)

Macromixing represents the bulk or convective mixing of fluids in a vessel. Mesomixing represents vortices created inside the bulk phase where both convective mixing and diffusion have an effect on interaction between lamellae (Baldyga J., 1998). The third and smallest time scale is micromixing and is limited by diffusion between lamellae. The total mixing time is a summation of the macro, meso and micro mixing time scales. The total time can be controlled by any one of these time scales. To determine the limiting time scale, an analysis of CFD simulations is required. This study hypothesizes that the mixing in these geometries creates vortices under the mesomixed time scale as suggested by Falk & Commenge (2010).

This study uses a reactive system and compares reactor geometries using "chemical rulers". A set of reactions known as the "Bourne reactions" have become the standard for mixing quantification and are extensively used in both batch and continuous systems to analyze the mixing efficiency. The Bourne reactions consist of several competing reaction with different reaction rates. The 4$^{th}$ Bourne reaction (Baldyga et al., 1998) tracks the

reaction rate of an acid base neutralization (reaction 1) by adding 2,2-dimethoxypropane (DMP) as an additive to the system (reaction 2).

$$NaOH + HCl \xrightarrow{k_1} NaCl + H_2O \quad (1)$$

$$\underbrace{CH_3C(OCH_3)_2CH_2}_{DMP} + H_2O + (H^+) \xrightarrow{k_2} \underbrace{(CH_3)_2CO}_{Acetone} + 2\ \underbrace{CH_3OH}_{Methanol} \quad (2)$$

Acid-base neutralizations are considered to be mixing dependant because the kinetics are so quick that they are limited by their rate of molecular interaction. In order to trace the rate of HCl consumption, the DMP is catalyzed by HCl resulting in a hydrolysis which produces stoichiometric amounts of acetone (AC) and methanol (MeOH). Figure 3.2 shows a schematic that explains how the reaction is able to trace mixing. When the mixing time is short relative to the characteristic reaction time of the slow reaction (2) (Figure 3.2 a), the system reaches a homogenous condition. Since $k_1$ is much greater than $k_2$, the HCl will be consumed too quickly for DMP to undergo hydrolysis and therefore AC or MeOH will not exist in detectable amounts. However, when the characteristic mixing time is greater or equal to the characteristic reaction time of the slow reaction (2), there exists a lamellar structure where a local concentration gradient exists. At the interface between two lamellae (Figure 3.2 b), NaOH will react immediately with HCl creating a NaOH depleted zone. The interface becomes rich with DMP, allowing it to hydrolyze with HCl (Johnson, & Prud'homme, 2003).

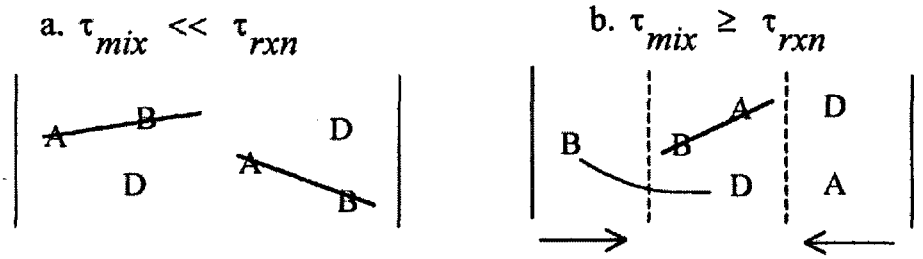


Figure 3.2: Depiction of reaction paths in mixing experiment (Johnson & Prud'home, 2003). $\tau_{mix}$ represents the characteristic mixing time and $\tau_{rxn}$ represents the characteristic reaction time. Here (A) would be the base, (B) the acid and (D) the DMP

In order to validate the reaction scheme as a chemical tracer for mixing, batch tests presented in Table 3-1, were performed and reflect conditions observed by Baldyga et. al. (1998). As expected, an increase in the stirring and thus mixing decreases the acetone yield as depicted in figure 3.2a where reaction 1 is strongly favored. The reaction scheme will now be implemented in a continuous micro reactor configuration.

Table 3-1: batch test to validate DMP hydrolysis

| Stirring Speed N/min | Acetone Yield % |
|---|---|
| 250 | 100% |
| 750 | 45% |

## 3.2. Experimental Setup

Experimental conditions and feed solutions were prepared based on the suggestion resulting from the batch experiments of Baldyga et al. (1998). Solutions were prepared with a minimum concentration of 0.1 mol/L of NaCl to ensure consistent kinetics of the neutralization and hydrolysis reactions (Dennison et al., 1976). The solution containing HCl was prepared with a concentration of 2000 ppm in a 25 %wt ethanol/water solution. The basic solution was prepared according to a 4:1 volumetric ratio between the alkali and acid solution. The concentration of NaOH in the basic solution yielded a 1.05 NaOH/HCl molar ratio to ensure that all the HCl was consumed at the reactor outlet. The alkali solution also contained the DMP additive which is essential to trace the HCl consumption. Similar to the acidic solution, the alkali solution was diluted with a 25%wt aqueous ethanol solution. Solvents were chosen to ensure that DMP remained soluble.

The two solutions were mixed using the TG, SZ and CAT mixing geometries (see figure 1.3). The total flow rate varied from 40 to 120 g/min to observe how the mixing structures create mixing at different Reynolds numbers and various degrees of secondary flow formation. Similar to the pressure drop experiments, flow rates were controlled by adjusting the power input of the gear pumps which were controlled using coriolis meters. Pressure measurements across the reactor plate were recorded with a Siemens PCS-7. Coiled pre-coolers were installed to ensure a constant temperature at the reactor inlet. The alkali solution was fed at higher flow rates and therefore a longer pre-cooler coil was installed to increase the residence time. Both the reactor plate and precoolers were placed

in a temperature controlled ethanol bath to ensure isothermal conditions. The configuration of the experimental setup can be found in figure 3.3.

Experiments performed in this chapter examine the effects mixing microstructure geometry, temperature, acid concentration, flow rate and viscosity on the methanol yield. Glycerol was found to greatly affect the solubility of DMP in the solution and therefore could not be used for this study. Polyethylene Glycol (PEG) with an average molecular weight of 8000 was used as a thickener since it could greatly increase the viscosity at a relatively small concentration, thus conserving the DMP solubility in the system. The viscous solutions were prepared with a concentration of 15% wt of PEG.

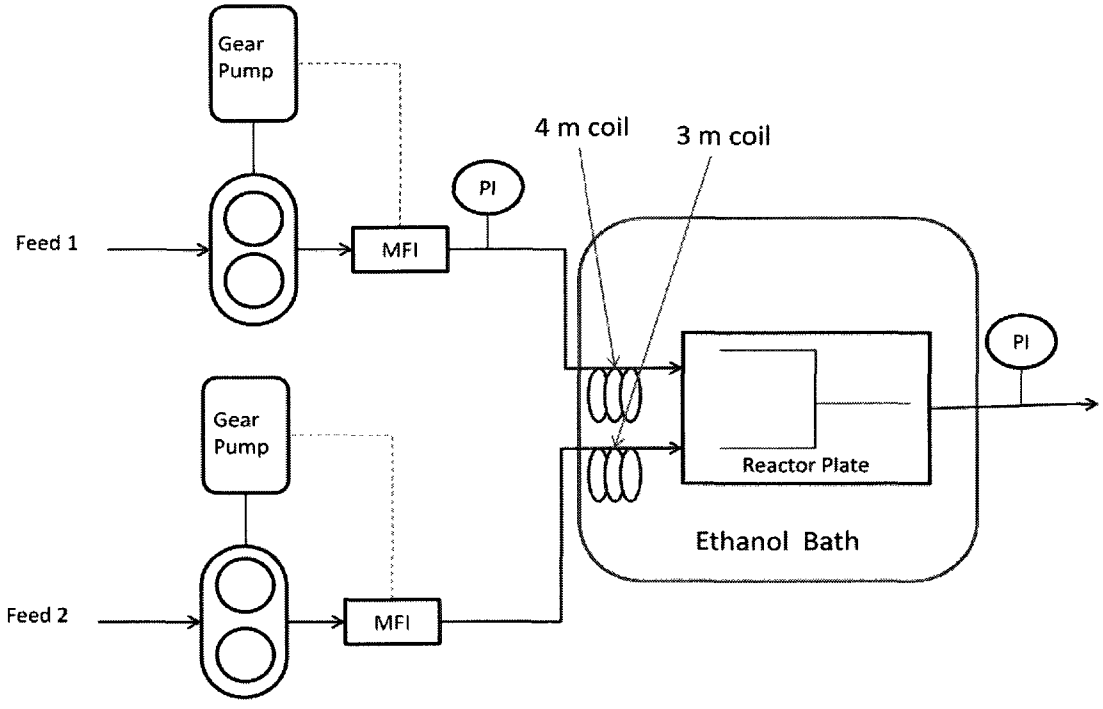


**Figure 3.3: Experimental setup of mixing experiments PI : Pressure Sensor, MFI: mass flow meter (coriolis meter)**

## 3.3. Results and Discussion

The effect of flow rate and system temperature on the methanol yield of the reaction scheme presented in section 3.1 is shown in figure 3.4. Increasing the flow rate requires an increase in energy input into the reactor by the pump. This effect was also seen in the pressure drop study in chapter 2. Furthermore, the increased velocity adds greater degree of lamellar instability, creating more intense secondary flows. More intense secondary flows stretch and cause greater mixing of the lamellae, creating an increased surface area between the two phases and a reduced distance for diffusion of NaOH. These effects increase interaction rate between NaOH and HCl and reduce the extent of DMP hydrolysis.

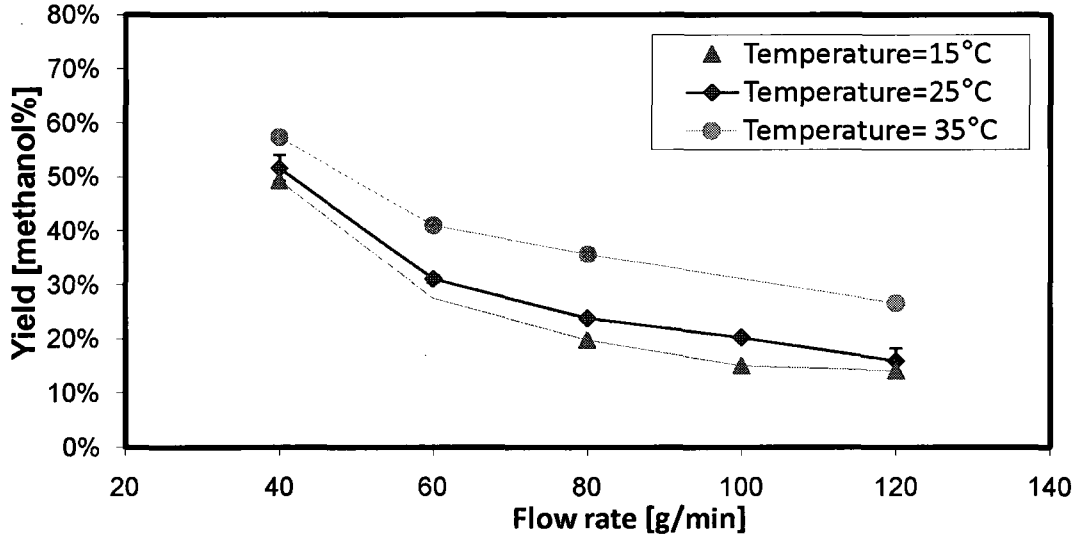


**Figure 3.4: Methanol yield at different flow rates and temperatures with a 100 series CAT reactor.**

There is also an effect of system temperature on the methanol yield. This is likely due to changes in the relative kinetics of DMP hydrolysis. From the Arrhenius relationship, an increase in temperature will increase the intrinsic rate constant ($k_r$).

$$k_r = A_r e^{-Ea/RT} \qquad (3.1)$$

The effect of temperature on the neutralization of HCl is small because this reaction is already very fast. However, the DMP hydrolysis reaction has a much slower intrinsic rate constant and therefore increasing the temperature has a greater effect on the reaction kinetics (Baldyga, et al., 1998).

Changing the operating temperature may also have an effect on the viscosity of the process fluid. Increasing the temperature would reduce the dynamic viscosity of the fluid and would and cause an increase in the Reynolds number, leading to a more turbulent system. However, pressure drop study in section 2.3 showed that the system is already creating a turbulent environment in the mixing zone, so reducing the viscosity will not have a significant effect on the degree of secondary flow formation. For this point to be valid the opposite trend of temperature would have been expected in Figure 3.4.

The effect of HCl concentration on the methanol yield can be seen in figure 3.5. Considerations should be given to the fact that all other system parameters, including stochiometry and volumetric flow rate ratios, are upheld. The rate of the neutralization reaction will increase due to increased amounts of HCl and NaOH.

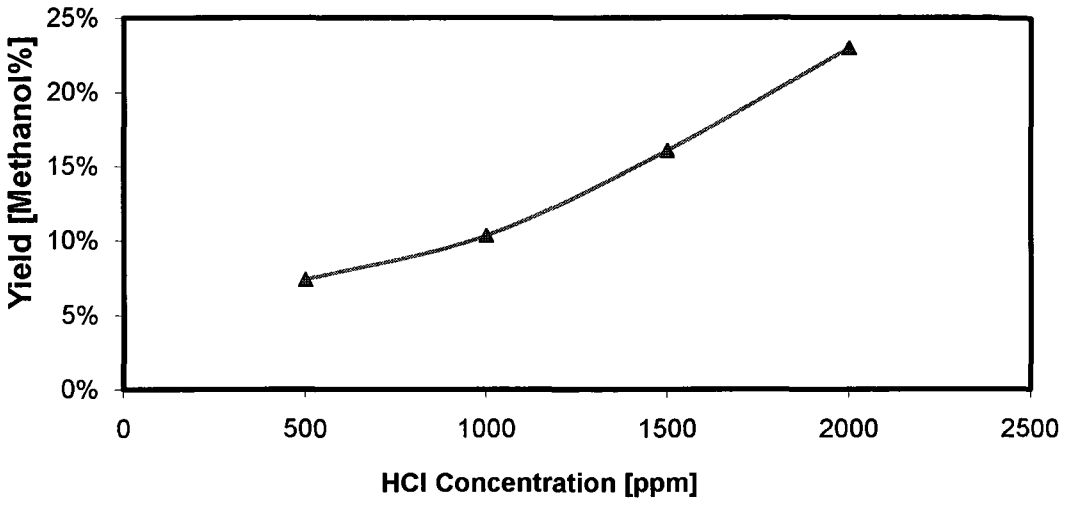


**Figure 3.5: Effect of HCl concentration of methanol yield , 100 series CAT mixing unit at 80 g/min total feed flow and 25 ˚C**

However, the constant stoichiometric ratio also increases the concentration of DMP in the system. There is therefore, a greater concentration of DMP at the phase interface, allowing for more DMP to be hydrolyzed by HCl.

With a good understanding of the effect of operating conditions on the reaction scheme, the effects of geometry and size can now be observed. Figures 3.6 to 3.8 present the methanol yield, at different flow rates, Reynolds numbers and pressure drops to observe the effect of geometry. Figure 3.6 shows different geometries, and various sizes of those geometries, at different flow rates. There is sufficient spreading which validates the chosen operating conditions in order to distinguish trends created by different geometries.

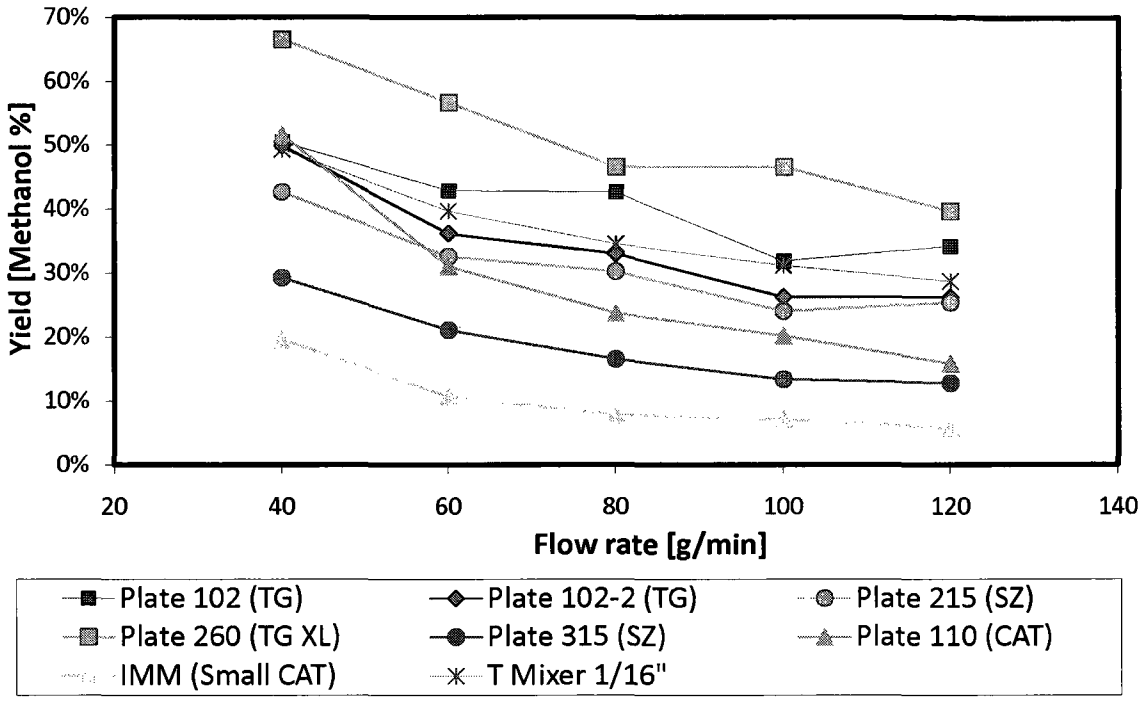


**Figure 3.6: Methanol yield vs. flow rate of various geometries at 25°C. Numbers represent the plate series ( 100, 200 and 300 ); TG represent a tangential mixing unit, SZ represents a SZ mixing unit, CAT represents a caterpillar mixing unit; TG XL represent an extra large tangential mixing unit.**

At a given flow rate and series, CAT geometries had the lowest methanol yield, SZ geometries had the second lowest methanol yield and TG geometries had the highest methanol yield for a given series. The smallest geometries of the 300 series presented the lowest methanol yields. At a given flow rate, smaller channels have higher velocities producing stronger secondary flows and better mixing. This effect is apparent in figure 3.7 where the methanol yield is presented versus the Reynolds number.

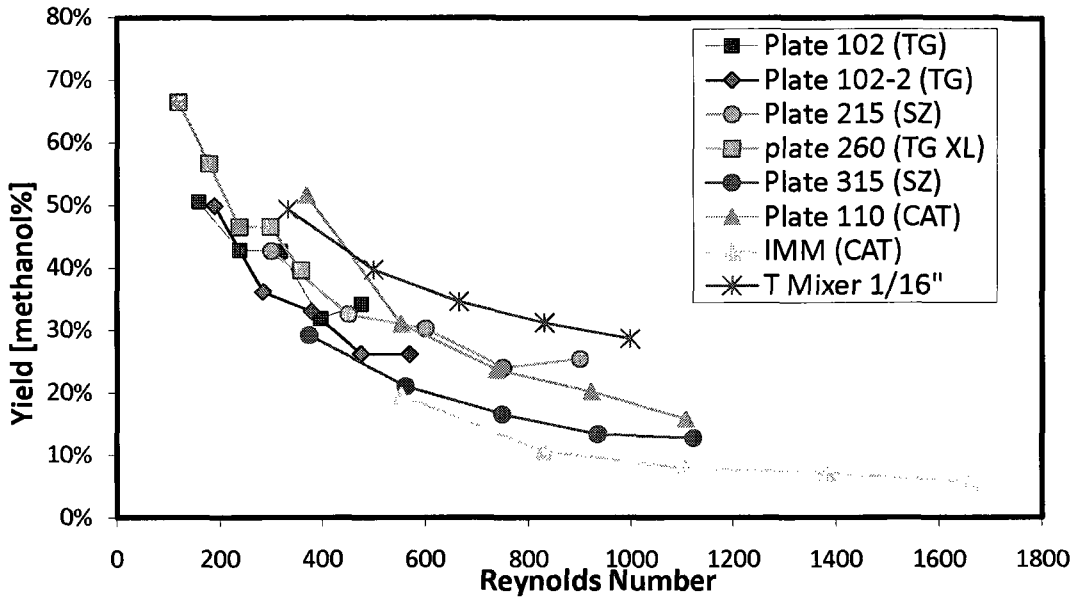


**Figure 3.7: Methanol yield Vs. Reynolds number with different geometries at 25℃. Numbers represent the plate series ( 100, 200 and 300); TG represent a tangential mixing unit, SZ represents a SZ shaped mixing unit, CAT represents a caterpillar mixing unit; TG XL represent an extra large tangential mixing unit.**

Increasing the Reynolds number increases the degree of turbulence in the flow field and results in lower methanol yields. Indeed, the smaller channel sizes in the CAT mixers and SZ mixing structures resulted in higher degrees of turbulence as their respective Reynolds numbers are higher. Similar to figure 3.6, CAT structures had the lowest methanol yield. However, the effects of geometry are less apparent. The Reynolds number alone cannot be used to compare geometries with respect to mixing efficiency because it does not reflect the intensity of the formed vortices. The vortex intensity is better represented by the pressure drop along the microreactor (see figure 3.8). As the pressure drop along the mixing zone increases the methanol yield decreases. The pressure drop is a representation of the energy being lost in system by wall friction and by vortex generation. Increasing the pressure gradient in the system forces the energy to dissipate faster, creating more intense vortices.

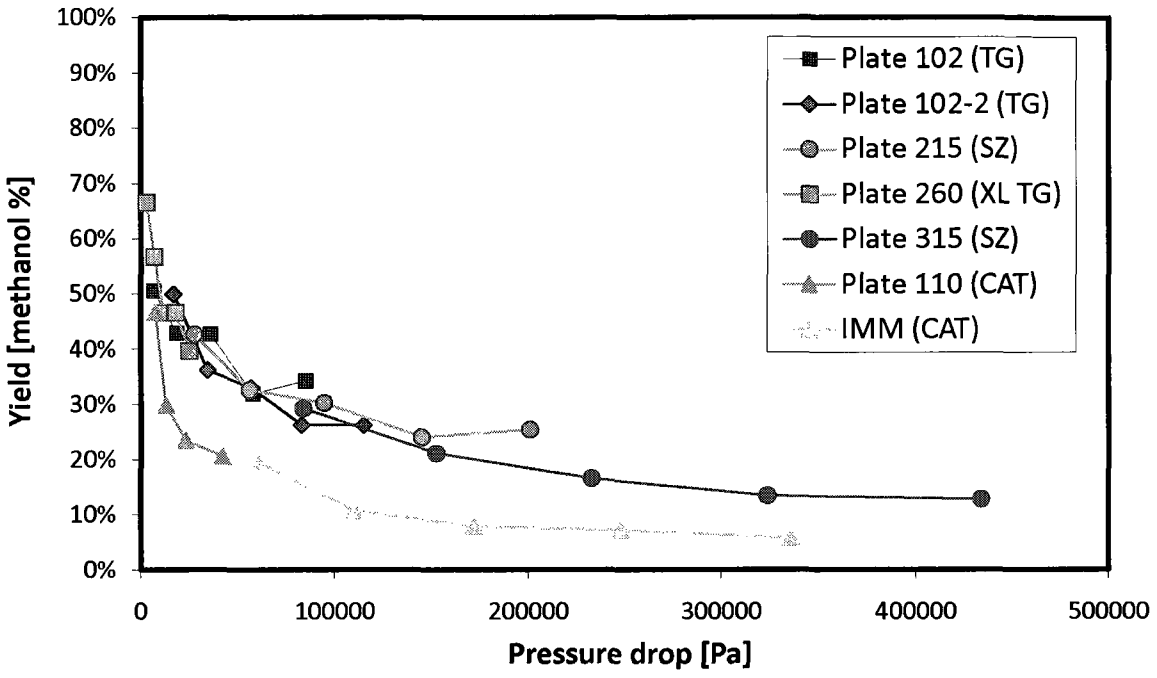


**Figure 3.8: Methanol yield vs. mixing zone pressure drop with different geometries at 25 ℃. Numbers represent the plate series ( 100, 200 and 300) ; TG represent a tangential mixing unit, SZ represents a SZ shaped mixing unit, CAT represents a caterpillar mixing unit; TG XL represent an extra large tangential mixing unit.**

Once again CAT structures had the lowest methanol yield at a given pressure drop. The small channel size of the CAT mixing unit not only creates a higher degree of turbulence relative to the other structures, as shown in Figure 3.7, but also forces the pumps to provide more energy to the system to overcome friction. Similar to figure 3.8, the effects of geometry is much less apparent, especially when comparing the SZ and TG mixing structures. However, there is a separate trend created by the CAT mixing structure, suggesting a possible geometric effect.

The product of the superficial velocity (linked to the degree of turbulence) and the pressured drop (energy input) results in the energy dissipation rate. The energy dissipation rate provides the rate at which the energy is dissolved by friction and the formation of

secondary flows. The energy dissipation rate is used to characterize mixing time, which facilitates the analysis of the mixing time in the system (Falk, et al., 2010). The geometries observed in this study have all proven to generate secondary flows via different mechanisms. Without CFD simulations, the mixing time scale for the geometries remains unknown. However, we can assume that these systems operate under the mesomixing time scale as both turbulent mixing and molecular diffusion play a role in this reaction scheme (Falk, et al., 2010). Since these geometries operate under the same time scale, the energy dissipation rate can be used to compare the mixing of several geometries on a common scale. The methanol yield versus the energy dissipation rate is presented in figure 3.9. Increasing the energy dissipation rate increase the mixing efficiency of the system as both the secondary flow generation and energy input into the system are increased.

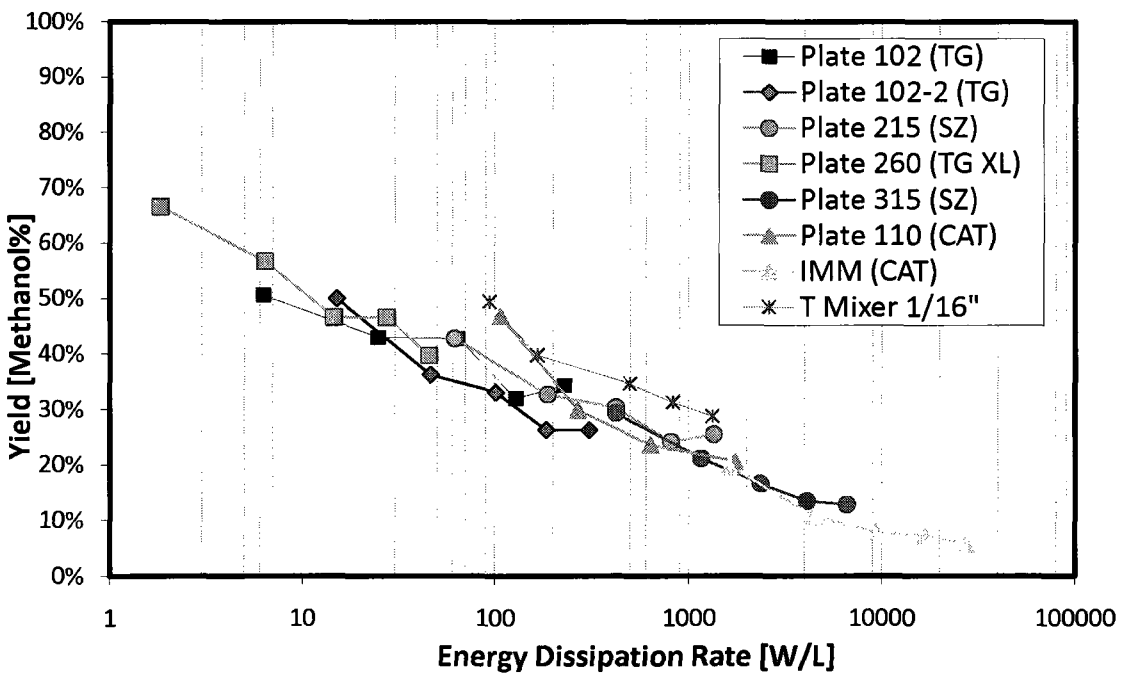


**Figure 3.9: Methanol yield Vs. energy dissipation rate with different geometries at 25°C. Numbers represent the plate series ( 100, 200 and 300); TG represent a tangential mixing unit, SZ represents a SZ shaped mixing unit, CAT represents a caterpillar mixing unit; TG XL represent an extra large tangential mixing unit.**

Figure 3.9 suggests that there is no distinguishable difference of the methanol yield between geometries at a given energy dissipation rate. The apparent trend presented in figure 3.9 also confirms the initial assumption that these geometries create vortices under the same time scale. When tested under turbulent conditions mixing is independent from geometry. However, this study cannot conclude that the flow patterns created by the different geometries do not present some advantage to mixing. Reaction schemes, for example homogeneous catalysts, may benefit from the axial mixing in the TG mixing structure. Exothermic and heat sensitive reactions may benefit from SZ or CAT geometries because reduced dead zone and axial mixing reduces the formation of hotspots along the reactor. Furthermore, the effect of viscosity likely plays a major role in the mixing of a system because the flow regime may change the limiting mass transfer in the reactor and the dominant mixing time scale.

### 3.3.1. Effect of Viscosity

Polyethylene Glycol was added to the standard solution to increase the viscosity from 2.0 cp to 10.03 cp. The viscosity was increased to observe its effect on the flow regime and the dominant mixing time scale. Indeed, the viscosity has an effect on several aspects of the system. First, the viscosity will reduce the Reynolds number because it is inversely proportional to the viscosity. As a result, the flow regime may become more laminar. The mixing time scale may become limited by molecular diffusion since the lack of turbulence reduces momentum based diffusion. Figure 3.10 presents the methanol yield

versus the energy dissipation rate at two different viscosities with similar flow rates. Initially there is a clear difference between the high and low (standard) viscosity systems. Values in the low viscosity system converge to a single trend, which is not apparent in the high viscosity system. Abrupt changes in the methanol yield is likely due to a transition from laminar to turbulent flow. (See figures 3.11 and 3.12)

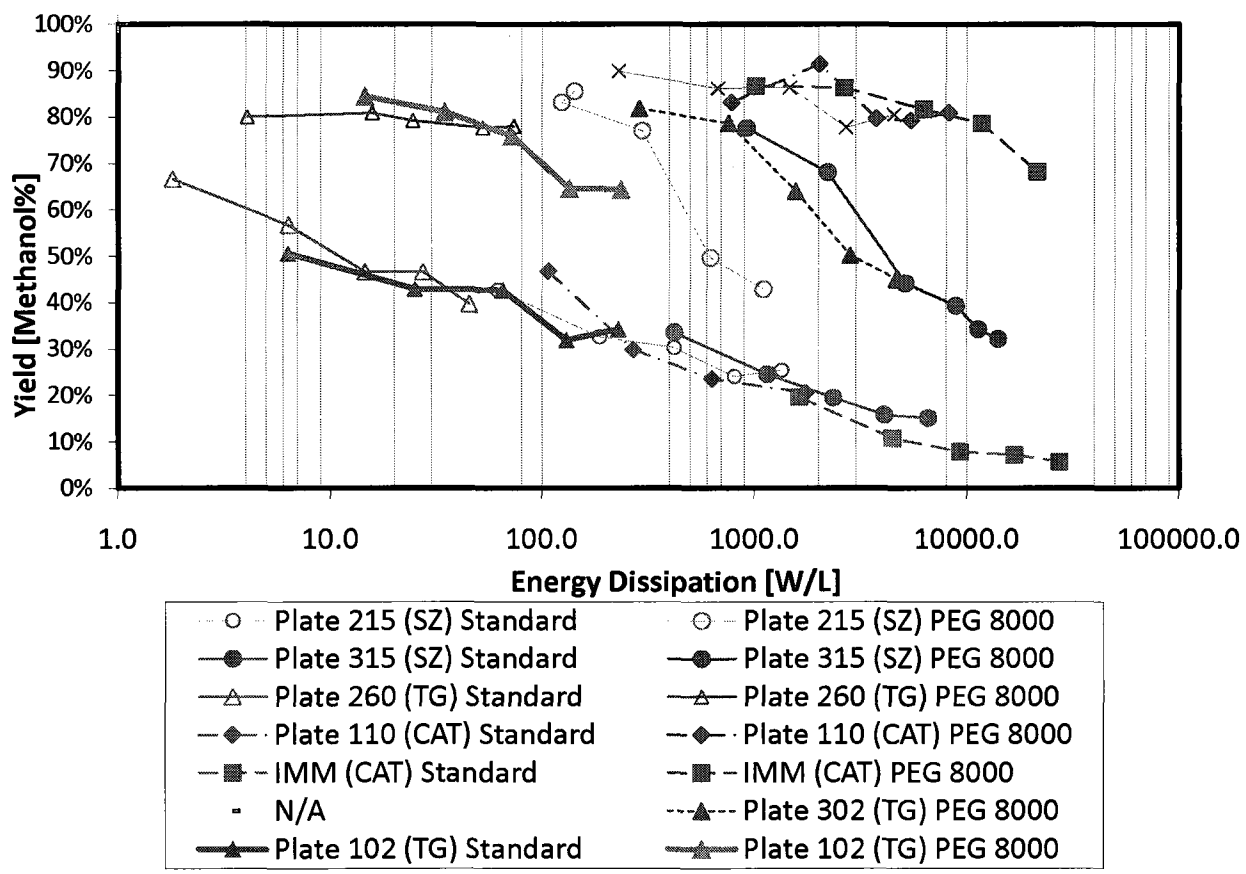


**Figure 3.10: Methanol yield vs. energy dissipation for various geometries under different viscosities , at a temperature of 25 ℃. Numbers represent the plate series (100, 200 and 300); TG represent a tangential mixing unit, SZ represents a SZ shaped mixing unit, CAT represents a caterpillar mixing unit; TG XL represent an extra large tangential mixing unit; "Standard" represents low viscosity results; "PEG 8000" represents high viscosity results**

Under laminar flow conditions, convective mixing is severely limited and therefore causes the mixing time scale to become limited by diffusion. To confirm the transition of the flow regimes, figures 3.11 and 3.12 demonstrates the relationship between the Reynolds number and pressure drop of selected reactors. Direct proportionality or linearity suggests a laminar flow regime whereas a non-linear relationship suggests a transitional or turbulent flow regime. In this case, a non-linear relationship suggests the creation of secondary flows akin to turbulence. A clear linear relationship is present in figure 3.11 as shown by the linear trend lines which corroborates with the performance of the two reactor plate (260-TG and 110-CAT) in figure 3.10. Under laminar flow conditions, the system remains controlled by diffusion with additional energy input having no significant effect on the methanol yield, i.e. There are no secondary flow patterns strengthening due to additional energy input. The methanol yield is high (80%) as HCl consumption is slowed by reducing the interaction rate and will therefore be available to catalyze the DMP hydrolysis reaction.

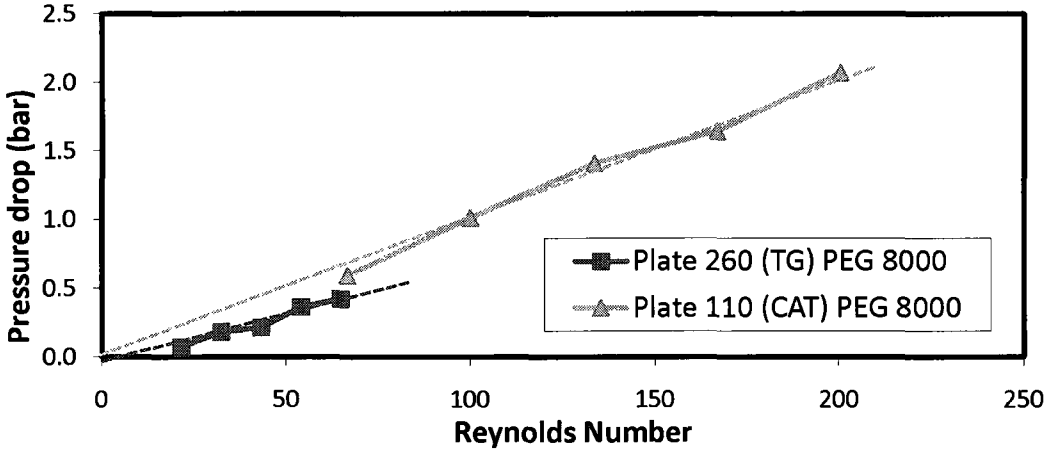


**Figure 3.11: Pressure Drop vs. Reynolds number of selected reactor with a linear relationship. Numbers represent the plate series (100, 200 and 300); TG represent a tangential mixing unit; CAT represents a caterpillar mixing unit; "PEG 8000" represents high viscosity results. Segmented lines show linearity.**

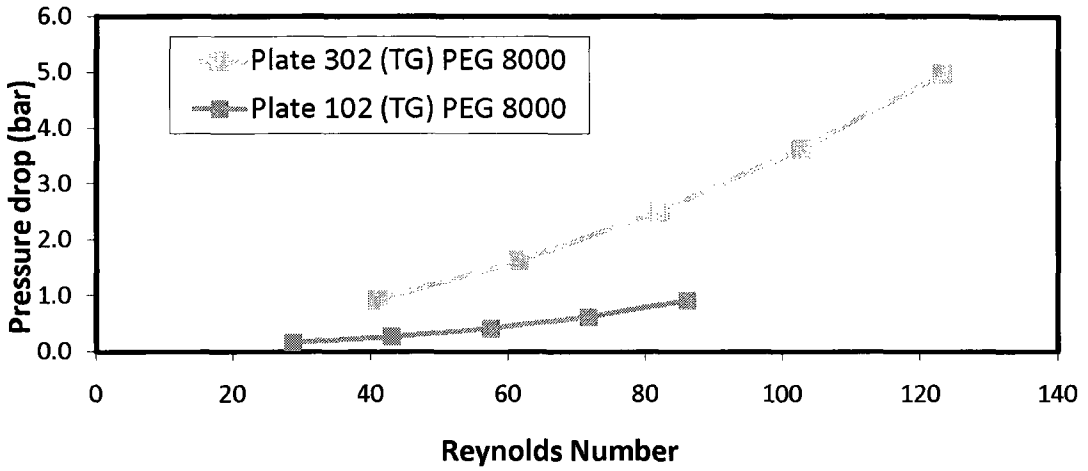


**Figure 3.12: Pressure Drop vs. Reynolds number of selected reactor with a non linear relationship. Numbers represent the plate series (100, 200 and 300); TG represent a tangential mixing unit; "PEG 8000" represents high viscosity results.**

Under turbulent conditions, the high viscosity trends should converge with the low viscosity trends as the systems are shown to be in similar time scales. The increase in energy dissipation due to viscosity, via an increased in the pressure drop, is factored out, see figure 3.13.

Under turbulent mixing conditions, both viscosities converge on a single trend confirming a system limited by the same mixing time scale. However, these reactor plates will converge at different point due to differences in their critical Reynolds numbers. The CAT mixing structures did not converge on this trend, which may be an effect of operating under laminar conditions. It is also possible the mixing zone did not have sufficient length to complete the NaOH neutralization because the CAT mixing units where significantly shorter than others in this study. TG and SZ mixing structures show the best mixing because they transition to a turbulent system. Under turbulent conditions, a single trend

emerges, adding confidence that the methanol yield and mixing efficiency are independent from geometry.

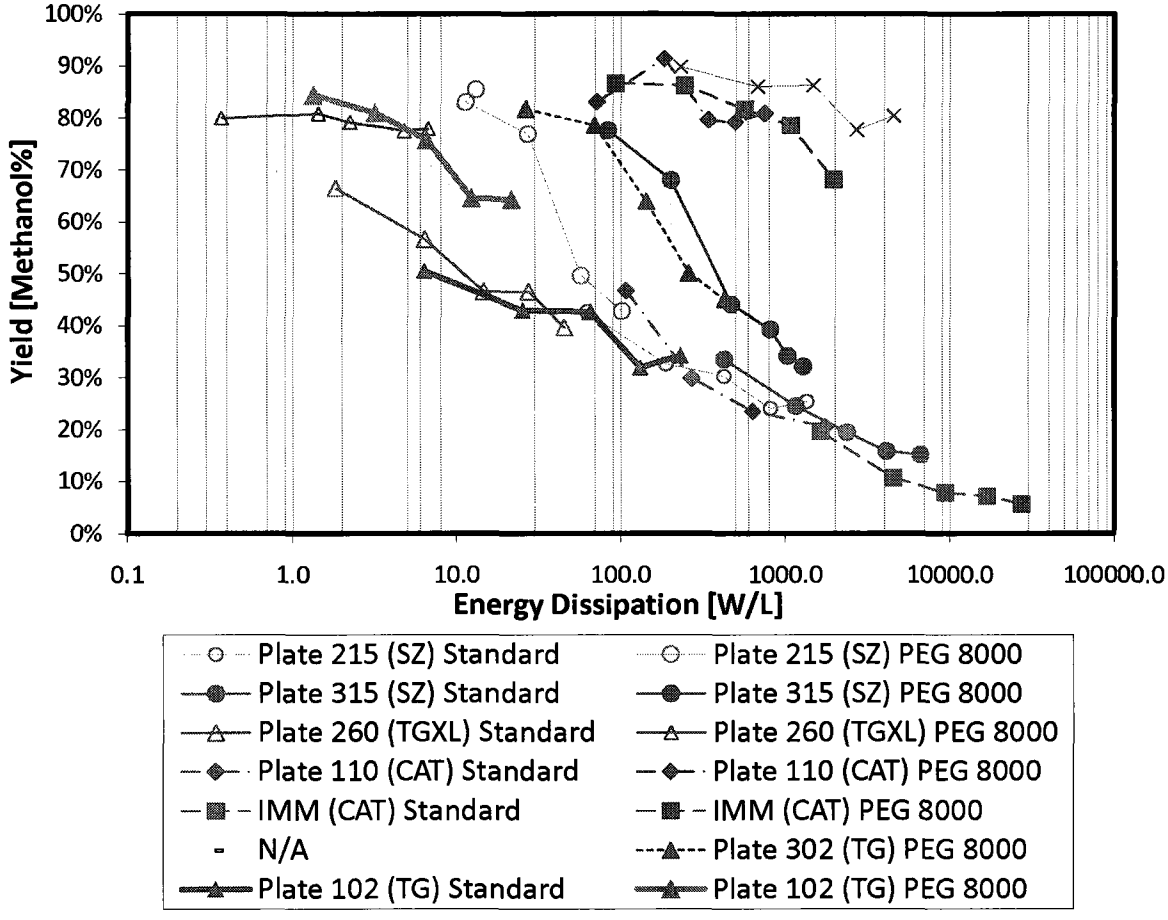


**Figure 3.13: Shifted viscous energy dissipation vs. methanol yield, The shift removes viscous effect of the pressure drop. Numbers represent the plate series (100, 200 and 300) ; TG represent a tangential mixing unit, SZ represents a SZ shaped mixing unit, CAT represents a caterpillar mixing unit; TG XL represent an extra large tangential mixing unit; "Standard" represents low viscosity results; "PEG 8000" represents high viscosity results.**

# Chapter 4. Heat Transfer Analysis

One of the main advantages of using microreactor technology is the heat transfer within the reactor. The heat transfer capabilities of microreactors exceed those of semi batch and batch processes significantly. As such, microreactors are being considered for many processes due to their heat transfer capabilities alone. Since many geometries are used in this technology, there are also several materials used as a basis for these geometries. Glass microreactors, for example, are often considered for their superior chemical resistance capabilities. However, glass is a poor heat conductor in comparison to metal reactors. This chapter performs a heat transfer analysis on two similar reactor plates made from two different materials to observe the effect of material on the overall heat transfer of a microreactor.

## 4.1. Heat Transfer Modelling

This chapter uses empirical modeling to determine the effect of different modes of heat transfer in a microreactor and to determine the overall heat transfer coefficient. Three modes of heat transfer are considered and the system is assumed to be perfectly insulated. The three types of heat transfer are shown in figure 4.1a and include the convective heat transfer of the process fluid ($U_{in}$), the conductive heat transfer across the reactor wall ($U_{wall}$) and the convective heat transfer of the thermal fluid ($U_{out}$).

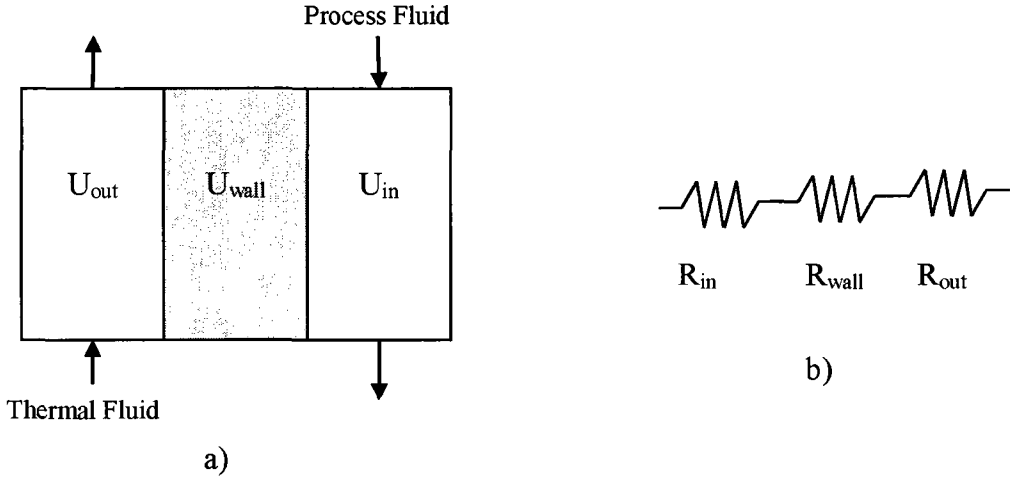


**Figure 4.1: a) Block diagram of modes of heat transfer in a microreactor channel; b) A thermal resistance from the process fluid to the thermal fluid.**

Figure 4.1b shows that the heat transfer is in series and the total resistance will therefore be the summation of the resistances. This includes the thermal resistance of the process fluid ($R_{in}$), the thermal resistant across the channel wall ( $R_{wall}$) and the thermal resistance of the thermal fluid ($R_{out}$). The summation of the resistances is shown in equation 4.1 (Incropera & DeWitt, 2002).

$$R_{Overall} = \sum R_i = R_{in} + R_{wall} + R_{out} \qquad (4.1)$$

The overall resistance converts to the heat transfer coefficient shown in equation 4.2 where the individual modes include geometrical effects .

$$\frac{1}{U_{Overall}} = \frac{1}{U_{in}} + \frac{1}{U_{wall}} + \frac{1}{U_{out}} \qquad (4.2)$$

The overall heat transfer coefficient was determined by dividing the log mean temperature difference by the average heat rate "q" (4.3) (Incropera & DeWitt, 2002). Experiments measured the inlet and outlet temperature of the process and thermal fluid.

$$U = \frac{q}{\Delta T_{lm} \cdot A_h} = \frac{q}{\left(\frac{\Delta T_2 - \Delta T_1}{\ln(\Delta T_2/\Delta T_1)}\right) \cdot A_h} \tag{4.3}$$

The heat transfer area "$A_h$" is constant for the geometries since they are considered similar. The heat transfer area is represented by the surface area at the top of the reactor because heat transfer in this setup only occurs on one side.

To determine the individual components of the overall heat transfer coefficient empirical models were applied. The heat transfer from the fluid to the reactor wall will be convective. Currently used relationships seen in figure 4.5 were found to be insufficient in providing a good fit to the experimental data. An empirical model was therefore chosen to represent the convective heat transfer of the process and thermal fluids, the effects of geometry on the convective heat transfer are unknown. Equations 4.4-4.6 represent empirical models for the process fluid (4.4), Thermal fluid of the Hastelloy reactor (4.5) and the thermal fluid of the Glass reactor (4.6).

$$U_{in} = H\dot{m} + I\dot{m}^2 \tag{4.4}$$

$$U_{out\ HC} = D\dot{Q} + E\dot{Q}^2 \tag{4.5}$$

$$U_{out\ Glass} = F\dot{Q} + G\dot{Q}^2 \tag{4.6}$$

The heat transfer of the process fluid ($U_{in}$) is assumed to be similar for similar geometries (see appendix C1). The two geometries will therefore be linked by constants "H" and "I". However, the thermal fluid channel of the microreactors examined in this study are different, therefore two sets of constant "D, E" and "F,G" are required.

Conduction is the main mode of heat transfer across the reactor wall and can be represented by equation 4.7, where k represents the material conductivity.

$$U_{wall} = Jk \tag{4.7}$$

The reactor geometries will be linked by "J" which is an empirical constants representing the geometric effects.

## 4.2. Experimental Setup

The experimental setup in this chapter uses a modular system known as the Siemens SiProcess (Siprocess, 2006). This modular system is an online control system with several modules with different uses. This heat transfer study uses a pumping module and a temperature control module. The pumps used were a dual piston pump module used by the SiProcess to control the process fluid flow rate. Flow rates of the process fluid ranged from 20 to 300 g/min of water. In addition to the SiProcess modules, a Huber heat exchanger was used to control temperature and thermal fluid circulation. The standard Huber thermal

fluid, known as "DW-Therm" (Synthesetechnik, 2005), was used as the thermal fluid for this study. Thermal fluid flow rates were chosen based on the pumping capabilities of the Huber heat exchanging unit and varied from 733 to 2200 g/min. Temperatures of the process and thermal fluids were monitored at the inlet and outlet of the microreactor. The process fluid inlet temperature remained constant at 25 ℃. Thermal fluid was set to three different inlet temperatures: 0 ℃, 60 ℃ and 80 ℃.

Two reactor plates with similar geometries were used to analyze the importance of materials on the heat transfer. The reactors in this study had tangential mixing structures, which differed in volume. Both reactors had the same main channel dimensions and the same overall reactor volume of 12 ml. Both reactors also had the same heat transfer area of 0.012 $m^2$ based on the surface of the reactor only on one side. Both sides of the reactor were well insulated to assume negligible heat loss. Details of the reactors used in this chapter can be found in Appendix C.

## 4.3. Results and Discussion

The results shown in figures 4.2 to 4.4 present the experimental data and modeled overall heat transfer coefficients with varying process and thermal fluid flows rates. Each figure represents a different thermal fluid inlet temperature. The model shown in each of the following figures provide a good fit where the correlation coefficients were greater than

0.99. The model constants are shown in Table 4-1, however the qualification of these values is not possible because they represent an empirical model.

**Table 4-1: Determined constants for Empirical Heat Transfer Model**

| Thermal fluid inlet temperature: | 0°C | 60°C | 80°C |
|---|---|---|---|
| H | 27.02 | 33.85 | 31.92 |
| I | -0.04 | -0.07 | -0.07 |
| J | 949 | 1182 | 1341 |
| D | 35.17 | 43.46 | 43.91 |
| E | -0.10 | -0.07 | -0.01 |
| F | 65.20 | 55.66 | 49.98 |
| G | 0.00 | 0.00 | -0.07 |

As the process fluid increases, the overall heat transfer coefficient will also increase due to an increasing internal heat transfer coefficient ($U_{in}$). The internal heat transfer coefficient increases due to an increase in the superficial velocity and Reynolds number. Increasing the thermal fluid flow rate also increases the overall heat transfer coefficient ($U_{overall}$), similar to effect seen in the process fluid.

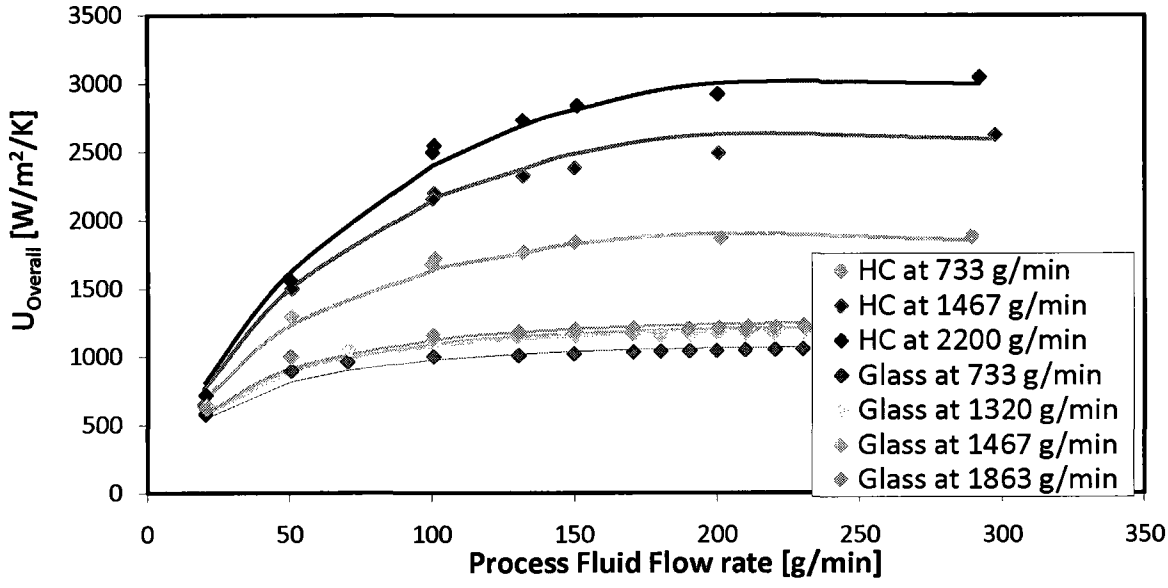


Figure 4.2: Overall heat transfer coefficient for glass and Hastelloy (HC) at 80 ℃; trends vary in the thermal fluid circulation rate. Model correlation coefficient ($R^2$): 0.990.

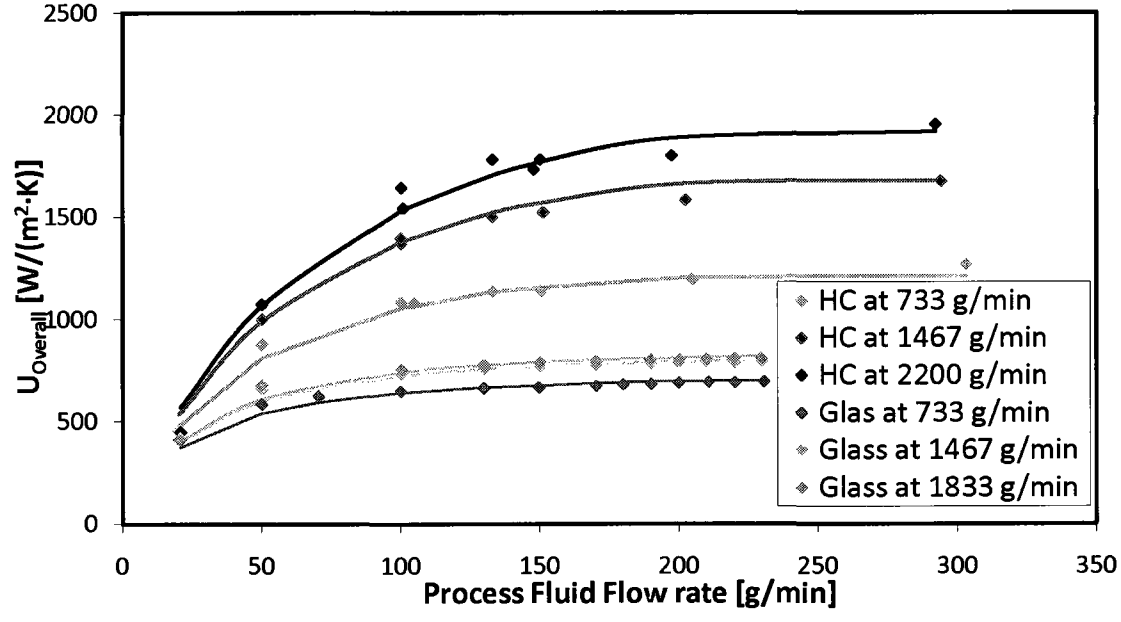


Figure 4.3: Overall heat transfer coefficient for glass and Hastelloy (HC) at 60 ℃; trends vary in the thermal fluid circulation rate. Model correlation coefficient ($R^2$): 0.991.

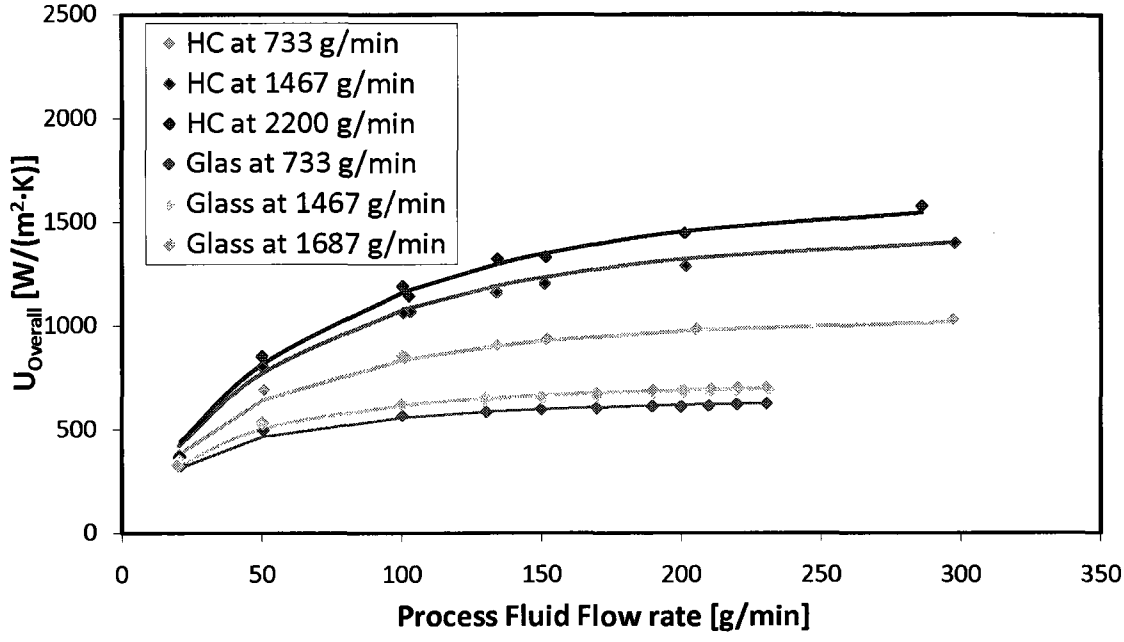


**Figure 4.4: Overall heat transfer coefficient for glass and Hastelloy (HC) at 0℃; trends vary in the thermal fluid circulation rate. Model correlation coefficient (R2): 0.995.**

The temperature of the system will have an effect on the heat transfer between the thermal and process fluid. The highest heat transfer rates are ordered highest to lowest; 80℃, 60℃ and 0℃. The change in fluid physical and thermal properties has a minor effect on the convective heat transfer coefficients, as opposed to the reduction in thermal conductivity through the reactor walls.

There is a clear distinction between the two materials observed in this heat transfer study. The Hastelloy reactor had a significant response to changes in the process and thermal fluid flow rates. This type of response suggests that both parameters have a significant effect on the overall heat transfer of the reactor, showing that the effect of material is not as significant in the heat transfer of this system. However, responses in the

glass structure were less pronounced and showed little response to an increasing process fluid flow rate and almost no response to an increase thermal fluid flow rate. The response in the glass system suggests that the material is limiting the heat transfer between the two fluids. However, the thermal fluid channel channels of the two microreactors had different geometries and dimension (Appendix C1) resulting in different velocities and heat transfer coefficients for a given flow rate

Figures 4.5 and 4.6 provide the internal and external heat transfer coefficients at various flow rates, temperatures, and materials. The internal heat transfer coefficient increases with increased process fluid flow rates because the Reynolds number causes an increase in convective heat transfer.

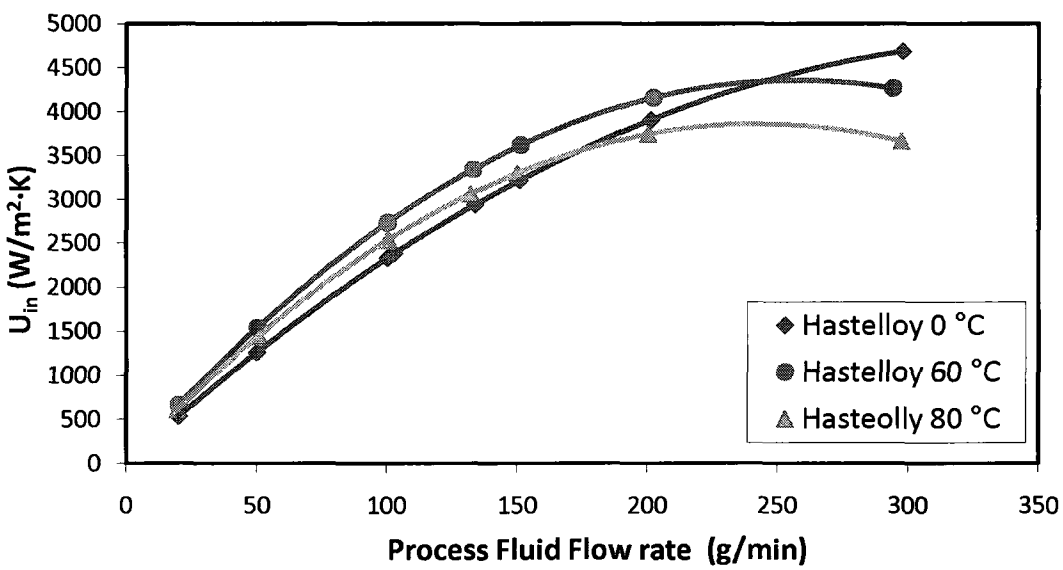


**Figure 4.5: Internal heat transfer coefficient at different temperatures and process fluid flow rates.**

As expected, there is no apparent difference between the internal heat transfer coefficients at different temperatures due to minor changes in the thermal and physical properties. There is however conflicting trend observed in figure 4.5. The internal heat transfer coefficient is over fitted because the appearance of a local maximum does not conform to the current understanding of this type of heat transfer. The occurrence of a local maximum at high flow rates is due to the polynomial fitting proposed in section 4.1. However, despite this over fitting at high flow rates, the model continues to show a good fit to the experimental data; as shown in figures 4.2-4.4. The geometry will also affect the internal heat transfer coefficient and might explain this counter intuitive result. It is not unreasonable to suggest that the effects of geometry create an optimal heat transfer rate. Indeed, factors such as pressure loss, friction and secondary flow formation will affect convective heat transfer.

Figure 4.6 plots the external heat transfer coefficient ($U_{out}$) at various thermal fluid flow rates, inlet temperatures, and materials. As expected, increasing the thermal fluid flow rate increases the Reynolds number which increases the convective heat transfer coefficient of the system. Additionally, it was not expected that the $U_{out}$ values in the glass and Hastelloy structures would converge as their heat exchange plates varied in geometry; glass channel being smaller in size (see Appendix C).

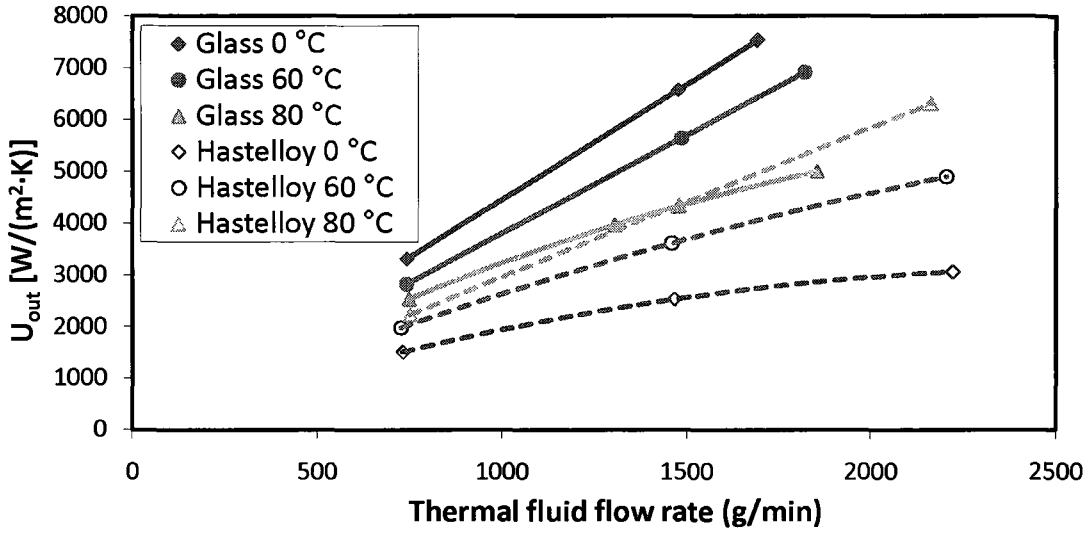


**Figure 4.6: External heat transfer coefficient at different temperatures, thermal fluid flow rates and reactor materials.**

However figure 4.6 shows an effect of temperature and a contradictory effect between the two reactor materials. The Hastelloy system proposes a proportional effect of temperature where an increase in the temperature also increases the exterior convective heat transfer coefficient. The glass system proposes an inversely proportional effect of temperature. The effect of temperature may be the result of significant changes in the fluid density and viscosity affecting the convective heat transfer but a similar effect would have been observed in figure 4.5 if that were the case. Low resolution, coupled with experimental error, is a more reasonable explanation for these contradictory trends.

The individual heat transfer mechanisms can now be compared to determine which are dominant. The percentage of resistance for the individual heat transfer mechanisms of each reactor at 60℃ is shown in figure 4.7. Figure 4.7 shows that as the process fluid flow

rate increases, the resistance associated with the internal heat transfer decreases. This is a result of the link between the convective heat transfer and the Reynolds number. Since the process fluid flow rate is the independent variable in figure 4.7, the relative resistances of the external channels and reactor wall will increase. The effect of material resistance for the Hastelloy system reached a maximum of 10%.

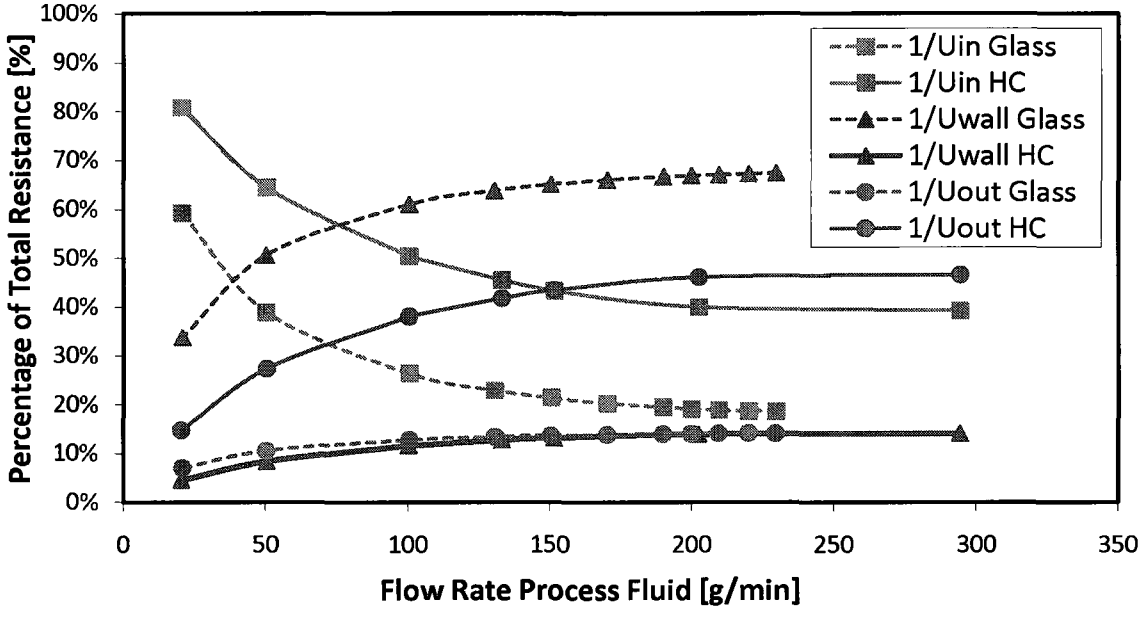


**Figure 4.7: Resistance of individual components on the overall resistance to heat transfer with a Hastelloy and glass reactor. The operating temperature is 60 ˚C and the thermal fluid circulation rate is 1467 g/min.**

At low process fluid flow rates, the internal resistance is dominant for both materials. However, the material becomes the dominant resistance for the glass reactor at flow rates above 50 g/min. The resistance of the glass reactor reaches a maximum of approximately 70%. Which illustrates that material conductivity can limit the heat transfer of a microreactor despite a large temperature driving force and small volumes. There is indeed a threshold where by the material conductivity can be considered the dominant resistance.

Based on the Reynolds number and creation of secondary flows by the geometry, the magnitude of the internal heat transfer will occur somewhere in between laminar and fully turbulent values and trends. This is confirmed by figure 4.8 where the proposed model was compared to currently used models at various process fluid flow rates. However, there are clear contradictions in the overall trend similar to the ones observed in figure 4.5 since it does not conform to our understanding of this type of heat transfer where one would expect the heat transfer to conform to laminar trends at lower flow rates and turbulent trends at higher flow rates. However, the magnitude of the internal heat transfer coefficient is acceptable considering the flow fields of different components.

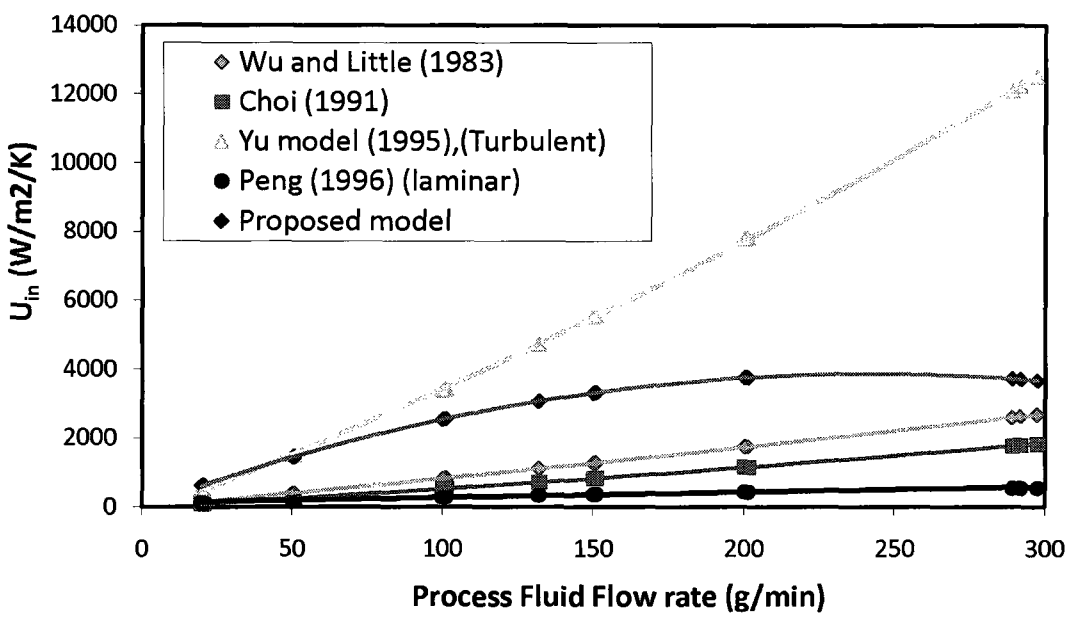


**Figure 4.8: Comparison of the proposed empirical model for $U_{in}$ to existing models for the Hastelloy reactor.**

Figure 4.7 demonstrates how the materials of construction affect the overall resistance to heat transfer and that the glass reactor is limited by the material conductivity while the Hastelloy reactor was limited by the internal and external heat transfer. Figure 4.9 shows the percentage difference between the heat transfer of the two reactors at different process and thermal fluid flow rates with Hastelloy as a base. At process fluid flow rates below 50 g/min the overall heat transfer is comparable as the glass reactor achieves between 75 and 85% of the Hastelloy's heat transfer capabilities. A similar effect is seen at the lowest thermal fluid circulation rate. As the process and thermal fluid flow rate increases, there is a drastic change in the heat transfer of the glass reactor due to its material conductivity, causing the overall heat transfer coefficient of the glass reactor to be less than 40% of that for the Hastelloy reactor.

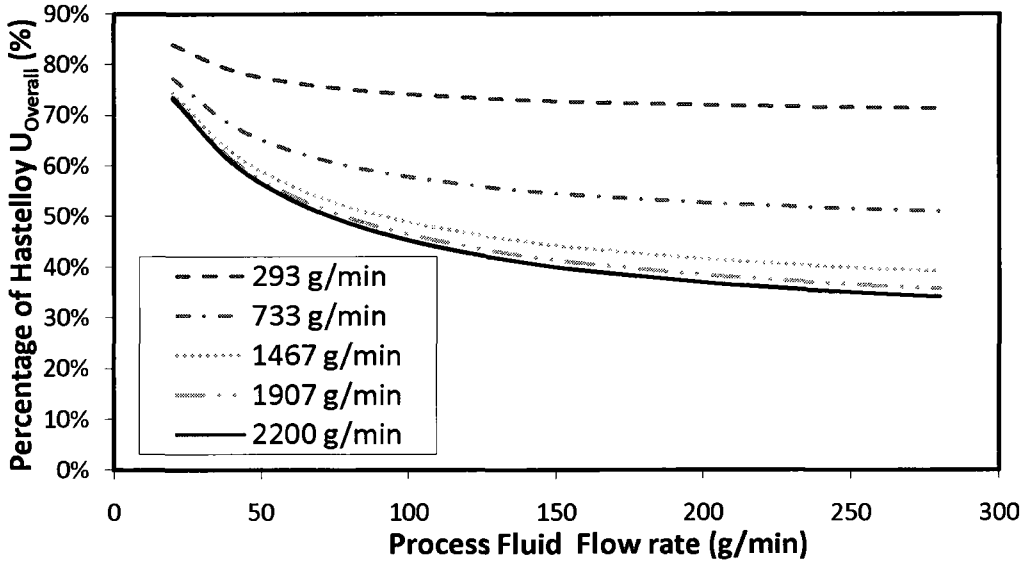


**Figure 4.9: Percentage difference of heat transfer for the glass and Hastelloy reactor as various process fluid flow rates. Different series represent various thermal fluid circulations rates show in the legend.**

Laboratories generally operate at lower flow rates thereby reducing the need for highly conductive materials. However, if microreactors are to be considered for industrial applications (Pont, 2009), operating conditions will include flow rates higher than 50 g/min. In that case, there is a clear advantage of using Hastelloy instead of glass, especially in reaction schemes heavily dependent on heat removal and operating temperature.

# Chapter 5. Conclusions and Suggestions for Future Work

Several processes used in the fine chemical and pharmaceutical industry have fast reactions. These fast reactions are shown to be mixing dependant, thus an important aspect in the characterization of microreactor geometries. The energy dissipation rate is a common representation of vortices in a pseudo turbulent flow regime. The energy dissipation rate links the pressure drop and superficial velocity to a single term. The pressure drop along the mixing zone is therefore needed to determine the energy dissipation rate and can be determined by friction factor modeling. Many applicable reactions are exothermic; their yield is therefore heavily dependent on the removal of hotspots formed at intense mixing zones. The heat transfer capabilities of certain reactor materials must therefore be analyzed to obtain an optimized process.

This study examined various effects of microreactor geometry and how they could be used to improve reactor performance and improve overall process efficiencies. Several reactor plates and mixing geometries were chosen to study the pressure drop and mixing efficiency of the microreactor. The chosen mixing geometries varied in their proposed mixing techniques. Tangential mixing provided mixing via creation of axial vortices; SZ shaped mixing unit used dean vortices to provide mixing; Caterpillar mixing structures used a split and recombine technique to mix the lamellae.

A pressure drop study, in Chapter 2, modeled several reactor plates with various components and sizes at different flow rates which allowed for an analysis of individual

components including different mixing geometries, main channels and reactor inlets and outlets. The model yielded an excellent fit where correlations coefficients exceeded 0.995. Analysis of the resulting constants, using a 95% confidence interval, suggested several model reductions and provided a qualification of the dominant flow regimes occurring in different components of the microreactor. It was found that the mixing zones and entrance and exits operated under turbulent conditions while the flat geometry of the main channel operated under laminar conditions even at elevated Reynolds numbers. However, this model was found to be greatly affected by the viscosity which reduced the predictability of the model outside the experimental range of the respective Reynolds numbers.

Following the pressure drop study, a reaction scheme was used as a "chemical ruler to compare the mixing of certain geometries on a common scale. The $4^{th}$ "Bourne" reaction was chosen; which links the extent of DMP hydrolysis through the consumption of HCL during and acid-base neutralization. The experimental trials showed that the mixing efficiency is independent of the mixing geometry under turbulent condition. Moreover, the three geometries tested in this study where shown to mix under the same time scale which was shown as all geometries could be compared using the energy dissipation rate. Increasing the viscosity was found to affect the critical Reynolds number of the system thus creating both laminar and turbulent flow regimes. Factoring out the viscous effect from the pressure drop shifted the energy dissipation rate where both high and low viscosity systems converged to a single trend. This study can conclude that the micro reactor mixing efficiency is independent from the geometry under turbulent conditions but does not

conclude that the mixing geometry does not matter as the flow field itself can affect the selectivity of various reaction schemes.

Finally the dependence of material was observed with an empirical model of the different modes of heat transfer in the reactor plate. The model yielded a good fit with a correlation coefficients greater than 0.99. However qualification of the modeled constants was not possible due to the nature of the empirical model. Material conductivity was shown have an effect on the overall heat transfer. However, there is a threshold where the effect of material conductivity becomes insignificant. The Hastelloy reactor provided up to 40% better heat transfer of the glass reactor plate and was limited by the convective heat transfer in the micro channel. The glass reactor was found to be limited by its material conductivity.

## 5.1. Suggestions for future work

This study on microreactor mixing and heat transfer could be enhanced by expanding the understanding of several aspects. This study determined that while the mixing efficiency is independent of the mixing geometry under turbulent conditions, the mixing geometry still has a significant effect on the process efficiency. Residence time distributions could be used to determine the degree of back mixing and effective reactor volume of different geometries. Reactor length studies would also be useful to analyze the breakthrough length of each mixing structure which would optimize the pressured drop along the reactor.

## Nomenclature

- A: Area of a square with dimension of $r_{MZ}$ x $r_{Mz}$
- a: Second intermediate stage in determining $V_{TC}$ (refers to figure B.4)
- $A_{1/4}$ :Area of a quarter of the tangential mixing zone
- $A_h$: heat transfer area
- $A_r$: pre exponential factor
- $A_{RST}$: Area difference between "A" and "$A_{1/4}$"
- B: Third intermediate stage in determining $V_{TC}$ (refers to figure B.4)
- C: Fourth intermediate stage in determining $V_{TC}$ (refers to figure B.4)
- CAT: Caterpillar mixing structure
- $C_f$: Channel Friction Factor
- CFD: Continuous flow dynamics ( refers to type of modelling)
- d: Diameter
- D: Empirical factor
- $d_h$: Hydraulic diameter
- E: Empirical factor
- Ea: Activation energy
- F: Empirical factor
- *f*: overall friction factor
- G: Empirical factor
- h: Channel height
- H: Empirical factor
- I: Empirical factor
- J: Empirical factor
- *k*: Material conductivity
- $k_r$ : reaction rate constant
- l: Channel length
- $l_{Entrance}$: Entrance length
- $l_{eq,}$: Equivalent channel length

- $l_{Exit}$: Exit length
- $\dot{m}$: Mass flow rate
- MFI: Mass flow indicator
- $n_B$ : number of bends
- $n_{MIX}$ : Number of mixing zones in one repeatable unit
- $n_{MZ}$: Number of mixing units in a reactor.
- $n_S$: Number of straight sections in an SZ mixing unit
- PI: Pressure Indicator
- $P_{w,EE}$: Wetted Perimeter of the entrance and exit
- $P_{w,MC}$: Wetted Perimeter of the main channel
- $q$: Rate of heat transfer
- $\dot{Q}$: Volumetric flow rate
- R: Gas constant = 8.314 J/mol·K
- r: radius
- $r_1$:Extrior bend radius
- $r_2$: Interior bend radius
- Re: Reynolds number $= \rho \cdot d \cdot u/\mu$
- $R_{in}$ : Internal thermal resistance
- $R_{out}$ : External thermal resistance
- $R_{Overall}$: Overall thermal resistance
- $R_{wall}$ : Thermal resistance of the reactor wall
- SA : Surface area
- $SA_B$ : Surface area of a main channel bend
- $SA_{TC}$: Transfer channel surface area
- SZ: SZ shaped mixing structure
- TG: Tangential mixing structure
- $U_{in}$ : Internal heat transfer coefficient
- $U_{out}$ : External heat transfer coefficient
- $U_{Overall}$: Overall heat transfer coefficient

- $u_{Ref}$: superficial velocity
- $U_{wall}$ : Heat transfer coefficient of the reactor wall
- V: Channel volume
- $V_B$: Volume of a main channel bend
- $V_{Bend}$ :Volume of a Main channel bend
- $V_{exp}$: Experimental total volume
- $V_{MIX}$ : Volume of a repeatable mixing zone unit
- $V_{Other}$: Other reactor section not defined by straight section or bend section ( to be determine manually)
- $V_{RMZ}$ : Volume of one mixing zone repeatable unit
- $V_{Straight}$ : Volume on straight sections of the main channel
- w: Channel width
- XA: Cross sectional area
- $\Delta P$: pressure drop
- $\Delta T$: Temperature difference
- $\Delta T_{lm}$: Log mean temperature difference

**Suffixes**

- TG: tangential mixing structure
- SZ: SZ shaped mixing structure
- CAT: Caterpillar mixing structure
- MC : main channel
- MZ : mixing channel
- EE: Entrance and exit
- TC: Transfer channel
- *eff*: effective ( refers to appendix B2)
- HC: Hastelloy reactor
- Glass: Glass reactor

**Greek letters**

- $\theta$: First intermediate stage in determining $V_{TC}$ (refers to figure B.4)
- $\lambda$: laminar friction factor
- $\omega$: turbulent friction factor
- $\rho$: density
- $\mu$: dynamic viscosity
- $\tau_{mix}$: the characteristic mixing time
- $\tau_{rxn}$: the characteristic reaction time

## References


Baldyga J., B. J. (1998). Non-isothermal micromixing in turbulent liquids: theory and experiment. *Canadian Journal of Chemical Engineering , 76* (3), 641-649.

Baldyga, J., & Bourne, J. R. (1999). *Turbulent mixing and chemical reactions.* Wiley.

Bourne, J. R., & Maire, H. (1991). Influence of the kinetic model on simulating the micromixing of 1-naphthol and diazotized sulfanilic acid. *Industrial & Engineering Chemistry Research , 30* (6), 1385-1389.

Bourne, J. R., Lenzner, J., & Petrozzi, S. (1992). Micromixing in Static Mixers: An Experimental Study. *31*, 1216-1222.

Choi, S., Barron, R., & Warrington, R. (1991). Fluid flow and heat transfer in microtubes. *Micro-mechanical Sensors, Actuators, and Systems, ASME DSC 32* , 123-134.

Dennison, D. B., Gettys, G. A., Kubler, D. G., & . Shepard, D. (1976). Kinetic salt effects on the hydrolysis of benzaldehyde dimethyl acetal. *The Journal of Organic Chemistry , 41* (13), 2344-2348.

Falk, L., & J.-M.Commenge. (2010). Performance comparison of micromixers. *Chemical EngineeringScience , 65*, 405-411.

Incropera, F. P., & DeWitt, D. P. (2002). *Introduction to Heat transfer* (4th ed.). John Wiley & Sons Inc.

Johnson, K., & Prud'homme, K. (2003). Chemical Processing and Micromixing in Confined Impinging Jets. *AIChE Journal , 49* (9), 2264-2282.

Jongkwang, L., & Kwon, S. (2009). Mixing efficiency of a multilamination micromixer with consecutive recirculation. *Chemical Engineering Science , 64*, 1223-1231.

Kockmann, N. (2008). *TRANSPORT PHENOMENA IN MICRO PROCESS ENGINEERING.* Springer.

Kockmann, N., Kiefer, T., Engler, M., & Woias, P. (2006). Convective mixing and chemical reactions in microchannels, with high flow rates. *Sensors and Actuators B , 117*, 495–508.

Kukukovaa, A., Aubin, J., & Krestaa, S. M. (2009). A new definition of mixing and segregation: Three dimensions of a key process variable. *Chemical Engineering Research and Design , 87*, 633–647.

Lee, S. W., & Lee, S. S. (2008). Rotation effect in split and recombination. *Sensors and Actuators B , 129*, 364-371.

Nevers, N. D. (2005). *Fluid mechanics for chemical engineers.* McGraw-Hill.

Ottino, J. M., Ranz, W. E., & Macosko, C. W. (1979). A LAMELLAR MODEL FOR ANALYSIS OF LIQUID-LIQUID MIXING. *Chemical Engineering Science , 34*, 877-890.

Peng, X., & Peterson, G. (1996). Convective heat transfer and flow friction for water flow in microchannel structures. *International Journal of Heat and Mass Transfer , 39*, 2599-2608.

Pont, J. (2009). Continuous processing and microreactor technology: Emerging technologies at the forefront of change in pharmaceutical and fine chemical manufacturing. *Chimica oggi* , *27* (3), 3.

Reizner, J. R. (2004). Exposing Coriolis Mass Flowmeters' "Dirty Littel Secret". *Chemical Engineering Progress* , *100* (3), 24-30.

Roberge, D. M. (2004). An Integrated Approach Combining Reaction Engineering and Design of Experiments for Optimizing Reactions. *Organic Process Research & Development* , *8* (6), 1049-1053.

Roberge, D. M., Ducry, L., Bieler, N., & Zimmermann, B. (2005). Microreactor Technology: A revolution for the Fine Chemical and Pharmaceutical Industry? *Chemical Engineering & Technology* , 318-323.

Rosaguti, N., Fletcher, D., & Haynes, B. (2004). Laminar Flow in a Periodic Serpentine Channel. *15th Australasian Fluid Mechanics Conference.* Sydney Australia.

Schönfeld, F., Hessel, V., & Hofmann, C. (2004). An optimised split-and-recombine micro-mixer with uniform. *4*, 65-69.

Siprocess, T. (2006, 04 04). *Siprocess microprocess system: Innovative technology for the chemical and pharmaceutical industry.* (Siemens) Retrieved 12 11, 2009, from www.seimens.com: https://www.automation.siemens.com/_en/portal/html/news/publications/detail/ra/reference.htm?url=/content/10001666/en/as/Pages/PN200601-08-Mikroprozesssystem_Siprocess_Innovative_Technologie_fuer_Chemie_und_Pharma.xml

Synthesetechnik, D. (2005). *DW-Therm Thchnical fact sheet*. Retrieved 2009, from www.huber-usa.com: http://www.huber-usa.com/dynamic/service/support/c2781ecb90f6e691.pdf

Wu, P. L. (1983). Measurement of friction factors for the flow of gases in very fine channels used for microminiature refrigerators. *Cryogenics* , *24*, 273-277.

Yu, D., Warrington, R., Barron, R., & Ameel, T. (1995). An experimentaland theoretical investigation of fluid flow and heattransfer in microtubes. *Proceedings of ASME/JSME Thermal Engineering Joint Conference*, (pp. 523-530).

Yung-Chiang Chung, Y.-L. H.-P.-C.-C. (2004). Design of passive mixers utilizing microfluidic self-circulation in the mixing chamber. *Lab on a Chip* , *4*, 70-77.

# Appendix A Reactor Dimensions for Mixing Analysis

Table A-1: Mixing Structure Dimensions

| Plate Number | Mixing structure | Mixing Volume (ml) | Hydraulic Diameter (mm) | Mixing structure length (mm) |
|---|---|---|---|---|
| Plate 110 | **CAT** | 0.049 | 0.90 | 60 |
| Plate 302 | **TG** | 0.209 | 1.38 | 104 |
| Plate 315 | **SZ** | 0.134 | 0.71 | 214 |
| T mixer 1/16" | **N/A** | 0.035 | 1.27 | N/A |
| IMM | **Small CAT** | 0.025 | 0.60 | 69 |
| Plate 102 | **TG** | 0.761 | 2.04 | 178 |
| Plate 102-2 | **TG** | 0.761 | 1.85 | 178 |
| Plate 215 | **SZ** | 0.303 | 0.95 | 288 |
| Plate 260 | **TGXL** | 1.118 | 2.66 | 151 |

# Appendix B Reactor Calculated Dimensions

## B.1 Determination of Microreactor Volume

MAIN CHANNEL VOLUME

The Main channel volume can be determined by the dissection of individual parts and added together. General channel design is summarized in Figure B.1. The residence time module or "Main Channel" can be dissected into straight and curved sections.

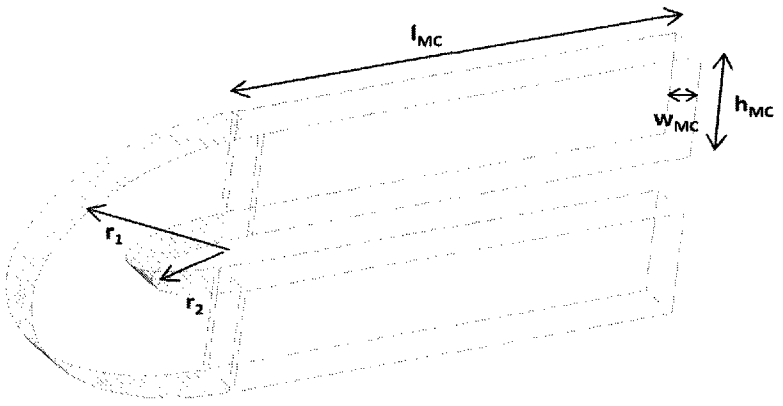


$l_{MC}$: main channel length
$w_{MC}$: main channel width
$h_{MC}$: main channel height
$r_1$:extrior bend radius
$r_2$: interior bend radius

**Figure B.1: General channel design**

### B.1.1 Sample Calculations of Channel Properties (Plate 102, (TG))

**Channel Cross sectional area($XA_{MC}$):**

$$XA_{MC} = h_{MC} * w_{MC} \qquad (B.1)$$

$$XA_{MC} = 10\ mm * 0.5\ mm$$

$$\boldsymbol{XA_{MC} = 5\ mm^2}$$

**Wetted Perimeter ($P_{W,MC}$):**

$$P_{W\,MC} = 2h_{MC} + 2w_{MC} \qquad (B.2)$$

$$P_{W_{MC}} = 2 * 10\ mm + 2 * 0.5\ mm$$

$$P_{W_{MC}} = \mathbf{21\ mm}$$

**Hydraulic diameter ($d_{h,MC}$):**

$$d_{h_{MC}} = 4 * \frac{XA_{MC}}{P_{W_{MC}}} \qquad (B.3)$$

$$d_{h_{MC}} = 4 * \frac{5\ mm^2}{21\ mm}$$

$$d_{h_{MC}} = \mathbf{0.95\ mm}$$

**Channel Friction Factor ($C_{f,MC}$) (Kockmann 2008):**

$$C_{f,MC} = 96 * [1 - 1.3553\alpha_A + 1.9467{\alpha_A}^2 - 1.7012{\alpha_A}^3 + 0.9564{\alpha_A}^4 - 0.2537{\alpha_A}^5] \qquad (B.4)$$

Where $\alpha_A = \frac{w_{MC}}{h_{MC}} \rightarrow \alpha_A = 0.05$

$$C_{f,MC} = 96 * [1 - 1.3553 * (0.05) + 1.9467 * (0.05)^2 - 1.7012 * (0.05)^3 + 0.9564 * (0.05)^4 - 0.2537 * (0.05)^5]$$

$C_{f,MC}$ =**89.94**

**Equivalent main channel length ($l_{eq,MC}$):**

$$l_{eq,MC} = \frac{V_{MC}}{XA_{MC}} = \frac{8505\ mm^3}{5\ mm^2} = 1701\ mm \qquad (B.5)$$

**Overall Length ($l_o$):**

$$l = \frac{V_{exp}}{XA_{MC}} = \frac{9580\ mm^3}{5\ mm^2} = 1916\ mm \qquad (B.6)$$

## B.1.2 Determining the Volume of Straight Sections

Straight sections are represented as rectangular prisms with a constant width. The volume ($V_{Straig\ ht}$) of straight portions of the main channel can be determined by the following.

$$V_{Straig\ ht} = w_{MC} * \sum_{i} l_{MC,i} * h_{MC} \qquad (B.7)$$

The channel height is also assumed to be constant so;

$$V_{Straig\ ht} = w_{MC} * h_{MC} * \Sigma_i\, l_{MC,i}$$

Where $\Sigma_i\, l_{MC,i} = l_{tot}$

**Sample calculations:**

$$V_{Straig\ ht} = 0.5\ \text{mm} * 10\ \text{mm} * 1514\ \text{mm}$$

$$\boldsymbol{V_{Straight} = 7570\ mm^3}$$

## B.1.3 Calculate Volume of Bends of the Main Channel

From figure B.2 to determine the surface area of the respective bend we subtract the surface area of the half circle produce by $r_2$ from the surface area of the half circle produce by $r_1$. The resulting surface area is then multiplied by the thickness of the micro-channel to result in its respective volume.

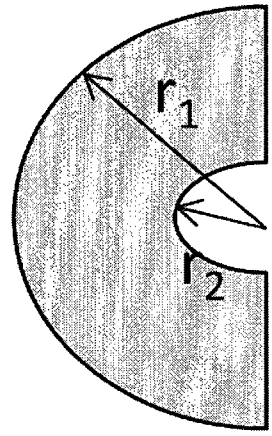


**Figure B.2: Calculation of surface area in channel bending**

***Sample calculation:***

$r_1$ =12 mm

$r_2$ =2 mm

$w_{MC}$ =0.5 mm

**Determine the surface area of the bend ($SA_B$):**

$$SA_B = \frac{\pi}{2} r_1^2 - \frac{\pi}{2} r_2^2$$

$$SA_B = \frac{\pi}{2}(12)^2 - \frac{\pi}{2}(2)^2$$

$$\boldsymbol{SA_B = 219.9\ mm^2}$$

**Determine the volume of the bend ($V_B$):**

$$V_B = SA_B * w_B$$

$$V_B = 219.9\ mm^2 * 0.5\ mm$$

$$\boldsymbol{V_B = 110.0\ mm^3}$$

**Determine total bend Volume ($V_{Bend}$):**

$$V_{Bend} = V_B * n_B$$

$$V_{Bend} = 110.0\, mm^3 * 8.5$$

$$\boldsymbol{V_{Bend} = 935\, mm^3}$$

Where $n_B$ represents the number of bends in the main channel

**Total Main Channel Volume:**

The total main channel volume ($V_{MC}$) consists of a summation of the bend volume and total straight volume. It is determined by the following calculation;

$$V_{MC} = V_{Bend} + V_{Straight} + V_{Other} \qquad (B.8)$$

$$V_{MC} = 880\, mm^3 + 7570\, mm^3$$

$$V_{MC} = 880\, mm^3 + 5\, mm^2 * 1514\, mm$$

$$\boldsymbol{V_{MC} = 8450\, mm^3}$$

## B.1.4 Tangentially Mixed Reactor

Transfer channel dimensions ( $l_{MZ}$ x $h_{MZ}$ ) : 0.875 mm x 0.785 mm

Reactor diameter ($d_{MZ}$ ) : 3.5 mm

Channel width ($w_{MZ}$) : 1.75 mm

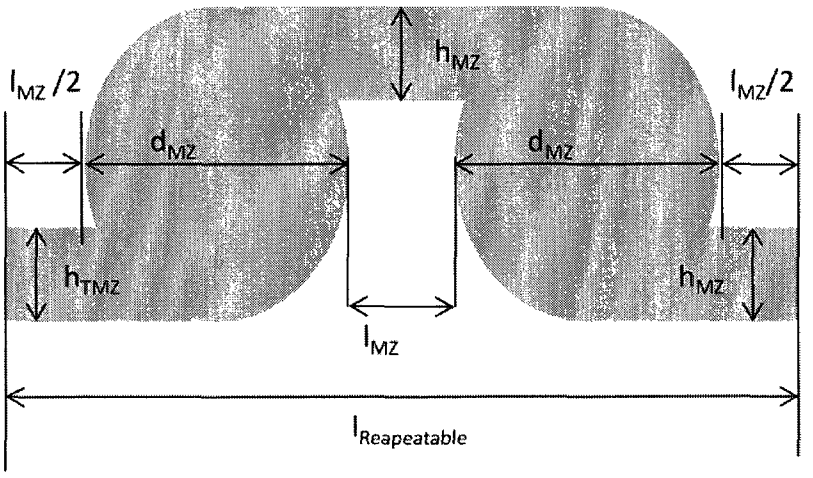


**Figure B.3: Tangential mixer repeatable unit**

## CALCULATE MIXING ZONE VOLUME:

Volume of a repeatable mixing zone unit ($V_{MIX}$)

$$V_{MIX} = n_{MIX} * \pi {r_{MZ}}^2 * w_{MZ} \qquad (B.9)$$

Where $n_{MIX}$ represents in the number of mixing zones in one repeatable unit. For a tangential mixing zone (Figure 3), $n_{MIX}$ =2

$$V_{MIX} = 2 * \pi * 1.75\ mm^2 * 1.75\ mm$$

Therefore $V_{MIX}$= **33.67 mm$^3$**

## CALCULATE TRANSFER CHANNEL VOLUME:

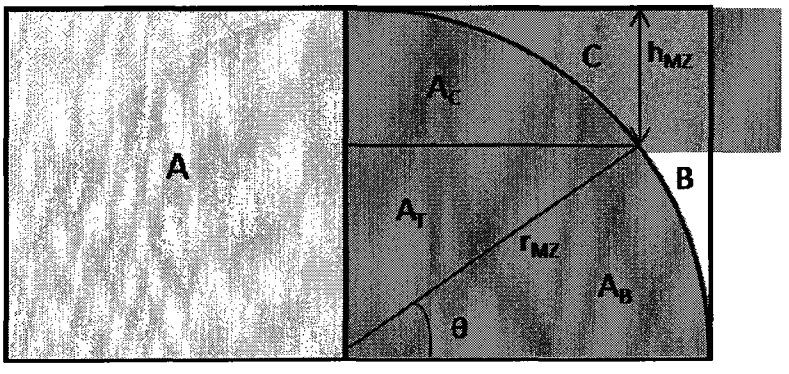


**Figure B.4: Determination of transfer channel transition surface area**

**Area of a square (A):**

$$A = {r_{MZ}}^2 = 1.75^2 = 3.0625\, mm^2$$

**Area of a quarter circle ($A_{1/4}$):**

$$A_{\frac{1}{4}} = \frac{\pi {r_{MZ}}^2}{4} = \frac{\pi * 1.75^2}{4} = 2.4053\, mm^2$$

**Area left over ($A_{RST}$):**

$$A_{RST} = A - A_{1/4} = 3.0625 - 2.4053 = 0.657\, mm^2$$

**Determine Area C:**

Area of a sector of a circle: $A_B = \frac{1}{2} {r^2}_{MZ} \theta$

Determine θ:

$$sin\theta = \frac{r_{MZ} - h_{MZ}}{r_{MZ}} = \frac{0.968}{1.75} \rightarrow \theta = 0.5861\, (radians)$$

Determine a:

$${r^2}_{MZ} = a^2 + (r_{MZ} - h_{MZ})^2$$

$$x = \sqrt{1.75^2 - 0.968^2}$$

$$x = 1.458\, mm$$

Calculate B:

$$B = (r_{MZ} - h_{MZ}) * r_{MZ} - A_T - A_B$$

$$B = (0.968 * 1.75) - \frac{1}{2}0.968 * 1.458 - \frac{1}{2}1.75^2(0.5861)$$

$B = 0.091$ mm$^2$

Determine Area C:

$$C = A_{RST} - B$$

$$C = 0.657\ mm^2 - 0.091\ mm^2 = \mathbf{0.566\ mm^2}$$

**TOTAL TRANSFER CHANNEL VOLUME FOR ONE REPETITIVE UNIT ($V_{TC}$)**

**(Figure B.3):**

**Determine the Cross Sectional area ($XA_{MZ}$):**

$$XA_{MZ} = h_{MZ} * w_{MZ}$$

$$XA_{MZ} = 0.78\ mm * 1.75\ mm$$

$$\boldsymbol{XA_{MZ} = 1.37\ mm^2}$$

Note: As the cross sectional are of the mixing zone varies, the applied cross sectional area refers to that of the transfer channels.

**Total surface area of transfer channels in one repetitive unit:**

$$SA_{TC} = 2 * (h_{MZ} * l_{MZ}) + 4 * C \qquad (B.10)$$

$$SA_{TC} = 2 * (0.875\ mm * 0.782\ mm) + 4 * 0.566\ mm^2$$

$$\boldsymbol{SA_{TC} = 3.633\ mm^2}$$

**Total volume of Transfer channels, $V_{TC}$:**

$$V_{TC} = SA_{TC} * w_{MZ} \qquad (B.11)$$

$$V_{TC} = 3.633\ mm^2 * w_{MZ}$$

$$V_{TC} = 3.633\, mm^2 * 1.75\, mm$$

$$\boldsymbol{V_{TC} = 6.357\ mm^3}$$

**TOTAL MIXING ZONE VOLUME:**

**Volume of one mixing zone repeatable unit($V_{RMZ}$):**

$$V_{RMZ} = V_{MIX} + V_{TC} \qquad (B.12)$$

$$V_{RMZ} = 33.67\ mm^3 + 6.357\ mm^3$$

$$\boldsymbol{V_{RMZ} = 40.03\ mm^3}$$

**Total mixing Zone Volume, $V_{MZ}$:**

$$V_{MZ} = V_{RMZ} * n_{MZ} \qquad (B.13)$$

$$V_{MZ} = 40.03\ mm^3 * 19$$

$$\boldsymbol{V_{MZ} = 760.51\ mm^3}$$

Where $n_{MZ}$ represents the number of repeatable units in the reactor

**Determine the equivalent length ($l_{eq}$):**

$$l_{eq,MZ} = \frac{V_{MZ}}{XA_{MZ}} \qquad (B.14)$$

$$l_{eq,MZ} = 760.51\ mm^3/1.37\ mm^2$$

$$\boldsymbol{l_{eq,MZ} = 556\ mm}$$

## B.1.5 S-Z Mixed Reactor Volume

Samples calculations refer to reactor model: Plate 215 (SZ)

Channel width($w_{MZ}$): 1.4 mm

Channel height ($h_{MZ}$) : 0.98 mm

Transfer channel length: ($l_{MZ}$): 2.8 mm

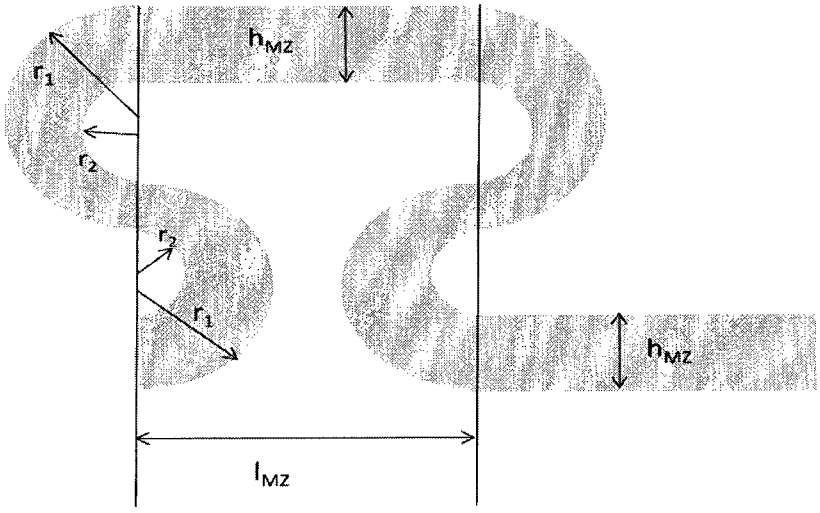


**Figure B.5: S-Z reactor design**

### CALCULATING THE BENDING VOLUME

S-Z reactor vessels, as found in figure B.5 consists of a changing overall channel thickness as created by off-centered radii. The reactor volume can be determined be a subtraction of the two surfaces.

***Sample calculation:***

$r_2$ =0.21 mm

$r_1$ =1.05 mm

$w_{MZ}$ =1.4 mm

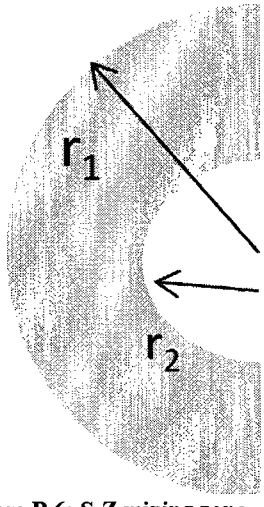


**Figure B.6: S-Z mixing zone bend diagram**

**Determine the surface area ($SA_{SZ}$):**

$$SA_{SZ} = \frac{\pi}{2} r_1^2 - \frac{\pi}{2} r_2^2$$

$$SA_{SZ} = \frac{\pi}{2}(1.05)^2 - \frac{\pi}{2}(0.21)^2$$

$$\boldsymbol{SA_{SZ} = 1.66\ mm^2}$$

**Determine the volume of the bend($V_{B,MZ}$):**

$$V_{B,MZ} = SA_{SZ} * w_{MZ}$$

$$V_{B,MZ} = 1.66\ mm^2 * 1.5\ mm$$

$$\boldsymbol{V_{B,MZ} = 2.49\ mm^3}$$

**DETERMINE TOTAL VOLUME OF ONE S-Z REPEATABLE UNIT:**

The total volume of one repeatable unit, as seen in figure B.5, consists of four variable height bend and two constant height straight channels. These individual components are summed up to determine the Volume of one S-Z repeatable unit.

**Determine the bend volume ($V_{MIX}$):**

$$V_{MIX} = n_B * V_{B,MZ} \qquad (B.15)$$

$$V_{MIX} = 4 * 2.33\ mm^3$$

$$\boldsymbol{V_{MIX} = 9.32\ mm^3}$$

**Determine the straight volume ($V_{TC}$):**

$$V_{TC} = n_S * h_{MZ} * l_{MZ} * w_{MZ} \qquad (B.16)$$

$$V_{TC} = 2 * 1.5\ mm * 2.8\ mm * 0.98\ mm$$

$$V_{TC} = 8.23\ mm^3$$

Where $n_s$ represents the number of straight channels in the mixing zone

**Determine the volume of one repetitive unit ($V_{RMZ}$):**

$$V_{RMZ} = V_{Mix} + V_{TC} \qquad (B.17)$$

$$V_{RMZ} = 9.32\ mm^3 + 8.23\ mm^3$$

$$V_{RMZ} = 18.21\ mm^3$$

## DETERMINE TOTAL VOLUME OF REACTOR ZONE (LV1-69474.215)

The total reactor unit consists of several repeatable units. In addition to the repeatable units, is an initial tangential mixing zone as found in figure B.7. Similarly to typical tangential mixing zones the volume can be determined using basic trigonometry found in figure B.4.

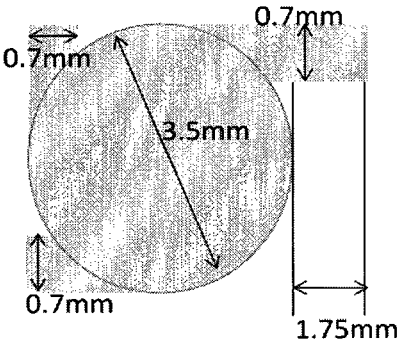


**Figure B.7: tangential mixing zone**

**Determine total reaction zone volume($V_{MZ}$):**

$$V_{MZ} = V_{RMZ} * n_{MZ} + V_{other} \qquad (B.18)$$

$$V_{MZ} = 17.0\ mm^3 * 18 + 17.00\ mm^3$$

$$V_{MZ} = 323\ mm^3$$

Where $V_{other}$ represents an estimated volume added by the initial tangential mixing zone.

## B.1.6 Entrance and Exit Volumes (Plate 102)

The sum of the entrance and exit volume ($V_{EE}$) is determined with the input and output channels of the respective plate. Both diffusers and contractions in at the respective inlet or output have been assumed negligible as there error associated with the calculation of the overall volume.

**Sample calculations:**

**Channel Cross sectional area($XA_{EE}$):**

$$XA_{EE} = \pi r^2{}_{EE} \qquad (B.19)$$

$$XA_{EE} = \pi(0.76\,mm)^2$$

$$\boldsymbol{XA_{EE} = 1.72\,mm^2}$$

Where $r_{EE}$ represents the inlet and outlet line radius

**Wetted Perimeter ($P_{W_{EE}}$):**

$$P_{W_{EE}} = 2 * \pi * r_{EE} \qquad (B.20)$$

$$P_{W_{EE}} = 2 * 0.76\,mm$$

$$\boldsymbol{P_{W_{EE}} = 4.65\,mm}$$

**Hydraulic diameter ($d_{h_{EE}}$):**

$$d_{h_{EE}} = 2 * r_{EE} \qquad (B.21)$$

$$d_{h_{EE}} = 2 * 0.76\,mm$$

$$\boldsymbol{d_{h_{EE}} = 1.48\,mm}$$

**Channel Friction Factor ($C_{f_{EE}}$) (Kockmann 2008):**

$$C_{f_{EE}} = 64$$

The channel friction factor represents flow in a pipe with a circular cross section.

**Equivalent main channel length $\left(l_{eq_{EE}}\right)$:**

$$l_{eq\,EE} = \frac{V_{EE}}{XA_{EE}} \qquad (B.22)$$

$$l_{eq\,EE} = \frac{120\ mm^3}{1.72\ mm^2}$$

$$l_{eq_{EE}} = 70\ mm$$

**Determine the total entrance and Exit volume ($V_{EE}$):**

$$V_{EE} = V_{Entrance} + V_{Exit} + \sum V_{EExtra} \qquad (B.23)$$

$$V_{EE} = XA_{EE} * l_{Entrance} + XA_{EE} * l_{Eexit} + 0$$

$$V_{EE} = 1.72\ mm^2 * 35\ mm + 1.72\ mm^2 * 35\ mm$$

$$V_{EE} = 120\ mm^3$$

Where $V_{EE}$ represents the total entrance and Exit volume, $\sum V_{EExtra}$ represents any other entrance volumes that may be present in the microstructure and $l_{Entrance/Exit}$ represents the respective entrance and exit lengths.

## B.2 Determination of TG average Channel Height

To determine the average height the effective surface area ($\overline{SA}_{eff}$) is divided by the length of the unit;

$$\bar{h}_{TG-eff} = \frac{\overline{SA}_{eff}}{l_{TG}} \qquad (B.24)$$

The average effective surface area is determined by adding the surface area of the sections $L_1$ and $L_2$ (see Figure B.8 ). Sample calculations are performed for plate 102.

$$\overline{SA}_{eff} = 2 \cdot \left( \int_{L_1}^{0} h_{TC-TG} dl + \int_{L_2}^{L_1} \sqrt{{r_{TG}}^2 - l^2} + r_{TG} dl \right) \quad (B.25)$$

$$\overline{SA}_{eff} = 2 \cdot \left( \int_{0.7295}^{0} 0.782 dl + \int_{2.1875}^{0.7295} \sqrt{1.75^2 - l^2} + 1.75 dl \right)$$

$$\boldsymbol{\overline{SA}_{eff} = 10.671\ mm^2}$$

Determine the average height ($\bar{h}_{TG-eff}$):

$$\boldsymbol{\bar{h}_{TG-eff} = \frac{10.671}{4.375} = 2.4391}$$

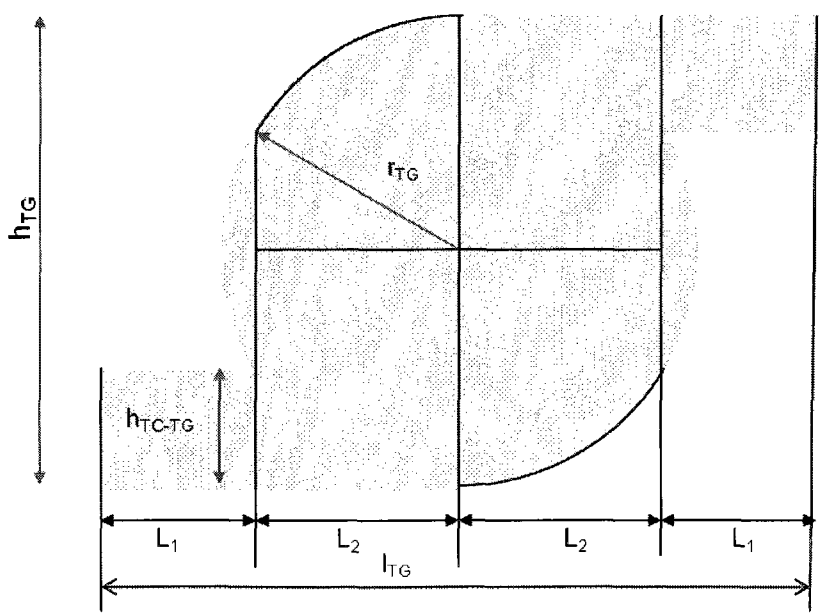


Figure B.8: effective surface area dimensions of Plate 102

# Appendix C Reactor Details for Heat Transfer Analysis

## C.1 Hastelloy Reactor

The Hastelloy reactor setup is found in figure C.1, The reactor plate details are as follows;

- Reactor volume ($mm^3$): 12000
- Reactor material conductivity (W/mK): 10.1
- Main channel dimensions (mm) (w x h): 2 x 5

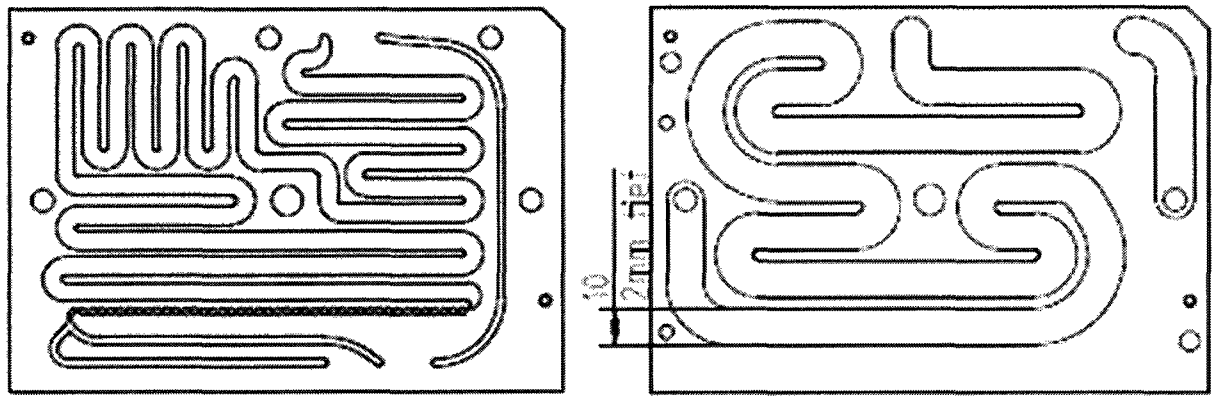


a) b)

**Figure C.1: The Haselloy reactor setup. a) is the reactor plate, b) is the heating/cooling plate.**

## C.2 Glass Reactor

The glass reactor setup is found in figure C.2, the reactor plate details are as follows;

- Reactor volume ($mm^3$): 12000
- Reactor material conductivity (W/mK): 1.05
- Main channel dimensions (mm) (w x h): 2 x 5

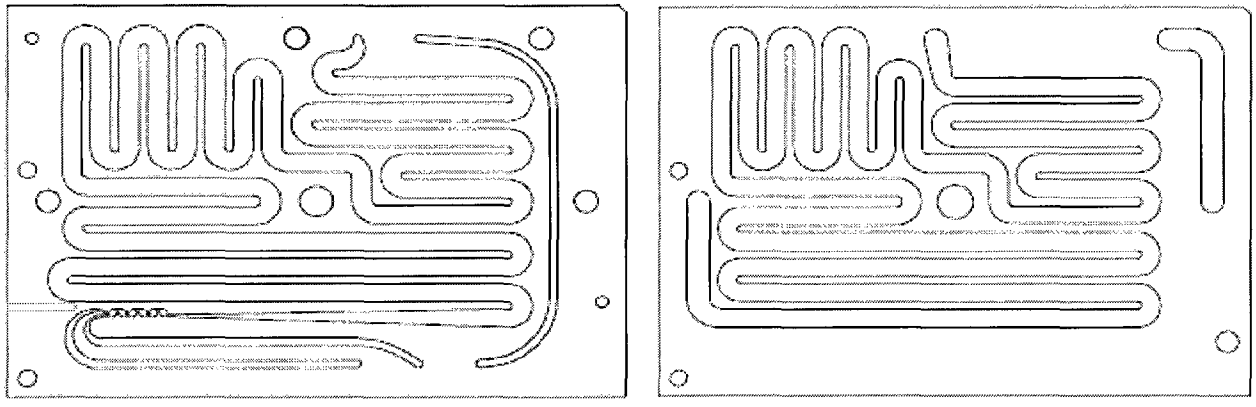

a) b)

**Figure C.2: The Glass reactor setup. a) is the reactor plate, b) is the heating/cooling plate.**